

Contents

2	1 Arcadia-MD1	2
3	1.1 The sensor	2
4	1.1.1 Two different FE flavor	3
5	1.2 Readout logic and data structure	3
6	1.2.1 Matrix division and data-packets	3
7	2 Characterization	7
8	2.1 TJ-Monopix1 characterization	7
9	2.1.1 Threshold and noise: figure of merit for pixel detectors	7
10	2.1.2 Linearity of the ToT	11
11	2.1.3 Calibration of the ToT	12
12	2.1.4 Changing the bias	16
13	2.1.5 Measurements with radioactive sources	18
14	2.1.6 Dead time measurements	23
15	2.2 ARCADIA-MD1 characterization	24
16	3 Test beam measurements	29
17	3.1 Apparatus description	30
18	3.1.1 Accelerator	30
19	3.1.2 Mechanical carriers	30
20	3.2 Measurements	31
21	Bibliography	36
22	Characterization of monolithic CMOS pixel sensors for charged particle detectors and	
23	for high intensity dosimetry	

²⁴ **Chapter 1**

²⁵ **Arcadia-MD1**

²⁶ [16] [17]

²⁷ Breve introduzione analoga a Monopix1 in cui descrivo brevemente la "timeline" da
²⁸ SEED Matisse a Md1 e Md2

²⁹ Tutti i minid, siano essi v1 o v2, sono Alpide like. Prima SEED si occupa di stu-
³⁰ diare le prestazioni: concept study with small-scale test structure (SEED), dopo arcadia:
³¹ technology demonstration with large area sensors Small scale demo SEED(sensor with em-
³² bedded electronic developement) Quanto spazio dato all'elettronica sopra il pwell e quanto
³³ al diodo. ..

³⁴ **1.1 The sensor**

³⁵ ARCADIA-MD1 is an LFoundry chip which implements the technology 110 nm CMOS
³⁶ node with six metal layer **??**. The standard p-type substrate was replaced with an n-type
³⁷ floating zone material, that is a tecnique to produce purified silicon crystal. (pag 299
³⁸ K.W.).

³⁹ Tra i wafer fabbricati finora ci sono 3 valori di spessore attivo nominale (lo spessore
⁴⁰ effettivo può variare di qualche micron ripetto a quello nominale): 48um, 100um e 200um.
⁴¹ In allegato un'immagine con le cross section.

⁴² Wafer thinning and backside lithography were necessary to introduce a junction at the
⁴³ bottom surface, used to bias the substrate to full depletion while maintaining a low voltage
⁴⁴ at the front side.

⁴⁵ C'è un deep pwell per - priority chain separare l'elettronica dal sensore; per controllare il
⁴⁶ punchthought è stato aggiunto un n doped epitaxial layer having a resistivity lower than
⁴⁷ the substrate. It is part of the cathegory of DMAPS Small electrode to enhance the signal

Parameter	Value
Matrix size	$\times \text{ cm}^2$
Pixel size	$25 \times 25 \mu\text{m}^2$
Depth	? μm
Electrode size	$9 \times 9 \mu\text{m}^2$
Power consumption	$\sim \text{ mW/cm}^2$

Table 1.1

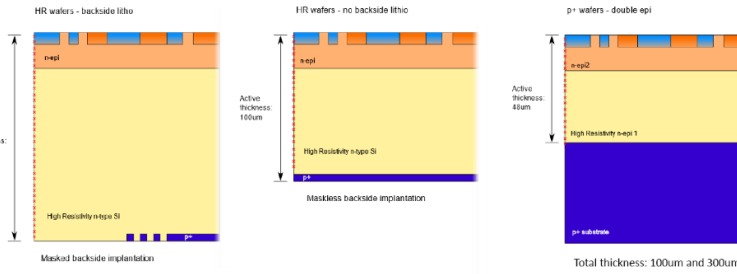


Figure 1.1

48 to noise ratio. It is operated in full depletion with fast charge collection by drift.

49 1.1.1 Two different FE flavor

50 Le differenze tra Alpide e bulk driven sono un po' più complesse di quanto hai scritto.
 51 Si tratta proprio di due architetture diverse. Il primo amplifica il segnale attraverso il
 52 trasferimento di carica tra due capacità. Nel bulk driven invece il guadagno è dato dal
 53 rapporto tra due transconduttanze. Inoltre ci sono altre differenze, il bulk driven è più
 54 sensibile alle cadute di tensione sul ground (che ahimè è esattamente ciò che accade nei
 55 dimostratori che abbiamo ora, a causa dell'anomalo consumo di corrente dal digitale,
 56 altro baco che abbiamo corretto nella terza sottomissione). Anche i livelli di tensione nei
 57 nodi interni dei due front-end differiscono e il meccanismo di clipping che funzionava per
 58 l'Alpide non è applicabile al bulk driven. Di conseguenza abbiamo un bias in più (ICLIP)
 59 nel secondo flavour per controllare il clipping. Nell'Alpide il clipping c'è, ma l'architettura
 60 usata permette di non aver bisogno di un bias esterno, anche se in una versione di Alpide
 61 di ALICE hanno scelto di controllare comunque la corrente di clip esternamente, per una
 62 maggiore flessibilità. Infine alcuni bias che hanno lo stesso nome nei due flavour, perché
 63 svolgono la stessa funzione, differiscono nel valore di configurazione didefault.

64 1.2 Readout logic and data structure

65 In order to achieve the lowest possible power consumption, the matrix is clockless, no
 66 free-running clock, and to save as much area as possible, it will not buffer any hits, and
 67 its readout will thus be triggerless.

68 The Periphery has both an analog part, segmented per Section, and a digital part,
 69 which is instead shared. The analog part hosts the bias cells for the AFE dei pixel, mentre
 70 la parte digitale che è unica per tutti riprocesso le hit che vengono dalle sezioni e 8b10b
 71 encode le parole per data transmission.

72 1.2.1 Matrix division and data-packets

73 The matrix is divided into an internal physical and logical hierarchy: The 512 columns are
 74 divided in 16 section: 512×32 pixels, each section has different voltage-bias + serializzatori.
 75 Each section is devided 512×2 column, and in 32×2 core: in modo che in ogni doppia
 76 colonna ci siano 1Pacchetto dei dati 6 cores. ricordati dei serializzatori: sono 16 ma
 77 possono essere ridotti ad uno in modalità spazio Ed infine regioni da 4×2 . The readout
 78 design must be capable of addressing the following matters Enough bus bandwidth for a

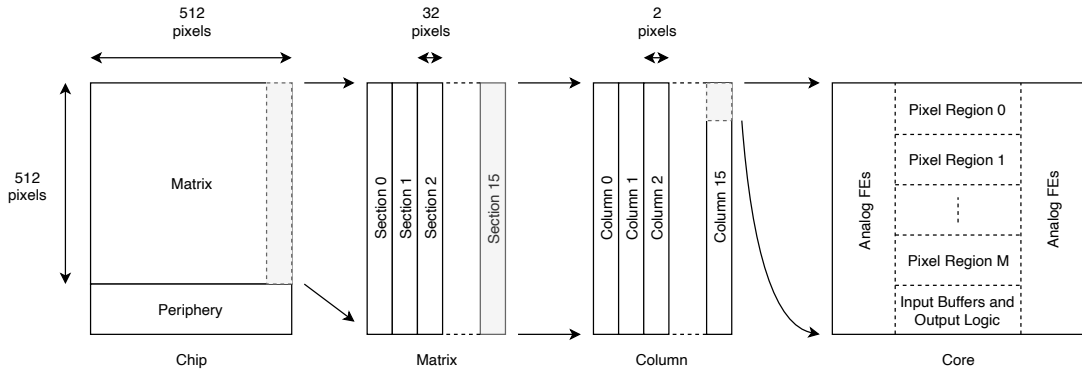


Figure 1.2

79 hit rate of 100 MHz/cm². Design decisions: Try and send as much data as possible to the
80 periphery (bandwidth) Lowest amount of logic possible (more routability)

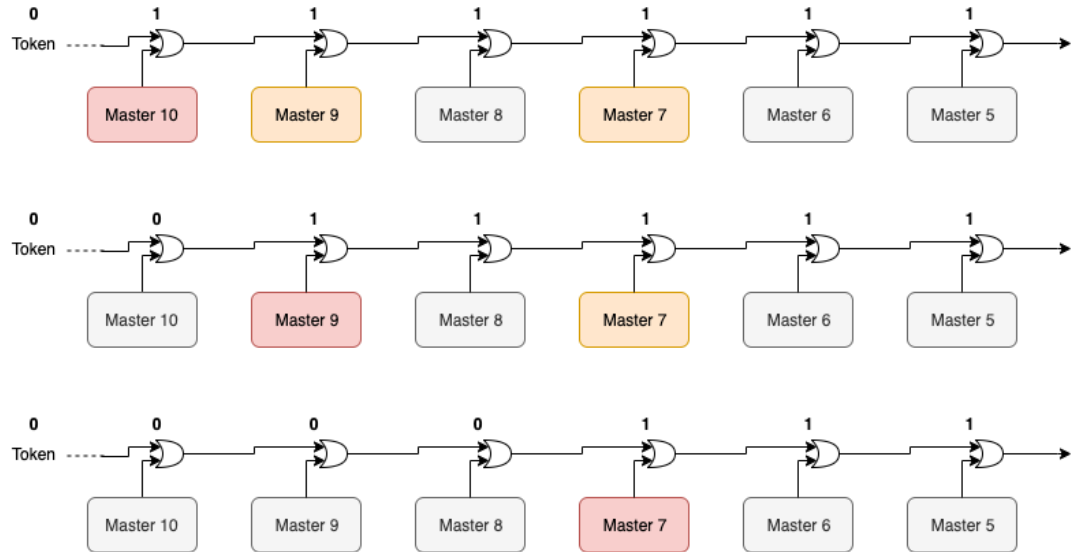


Figure 1.3

81 Questa divisione si rispecchia in come sono fatti i dati: scrivi da quanti bit un dato è
82 fatto e le varie coordinate che ci si trovano dentro; devi dire che c'è un pixel hot e spieghi
83 dopo a cosa serve, e devi accennare al timestamp

84 "A core is simply the smallest stepped and repeated instance of digital circuitry. A
85 relatively large core allows one to take full advantage of digital synthesis tools to imple-
86 ment complex functionality in the pixel matrix, sharing resources among many pixels as
87 needed.". pagina 28 della review.

88

89 TABELLA: con la gerarchia del chip Matrix (512x512 pixels) Section (512x32 pixels)
90 Column (512x2) Core (32x2) Region (4x2)

91 Nel chip trovi diverse padframe: cosa c'è nelle padframe e End of section.

92 "DC-balance avoids low frequencies by guaranteeing at least one transition every n
93 bits; for example 8b10b encoding n =5"

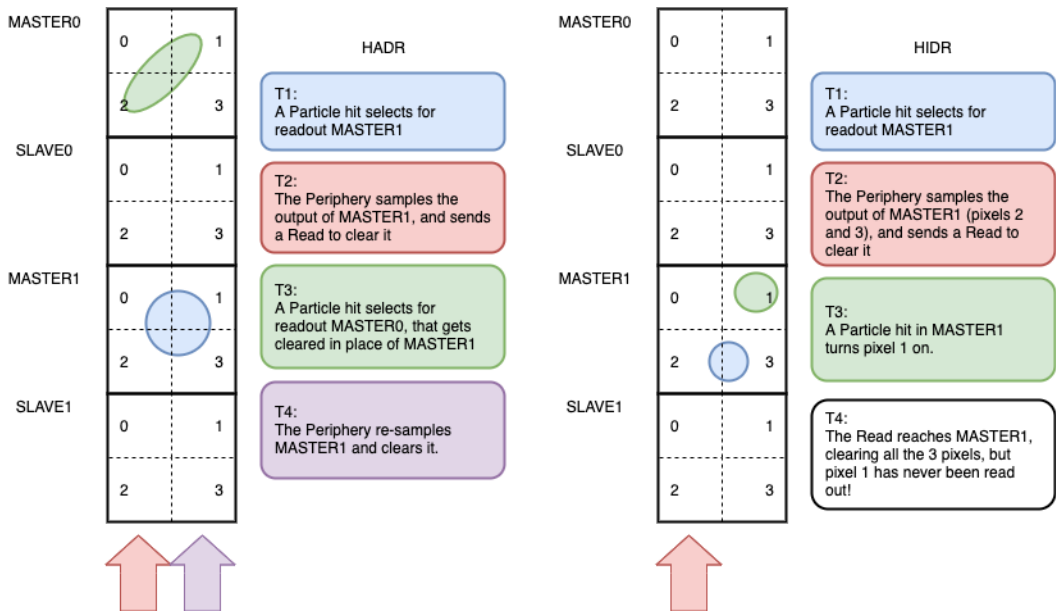


Figure 1.4

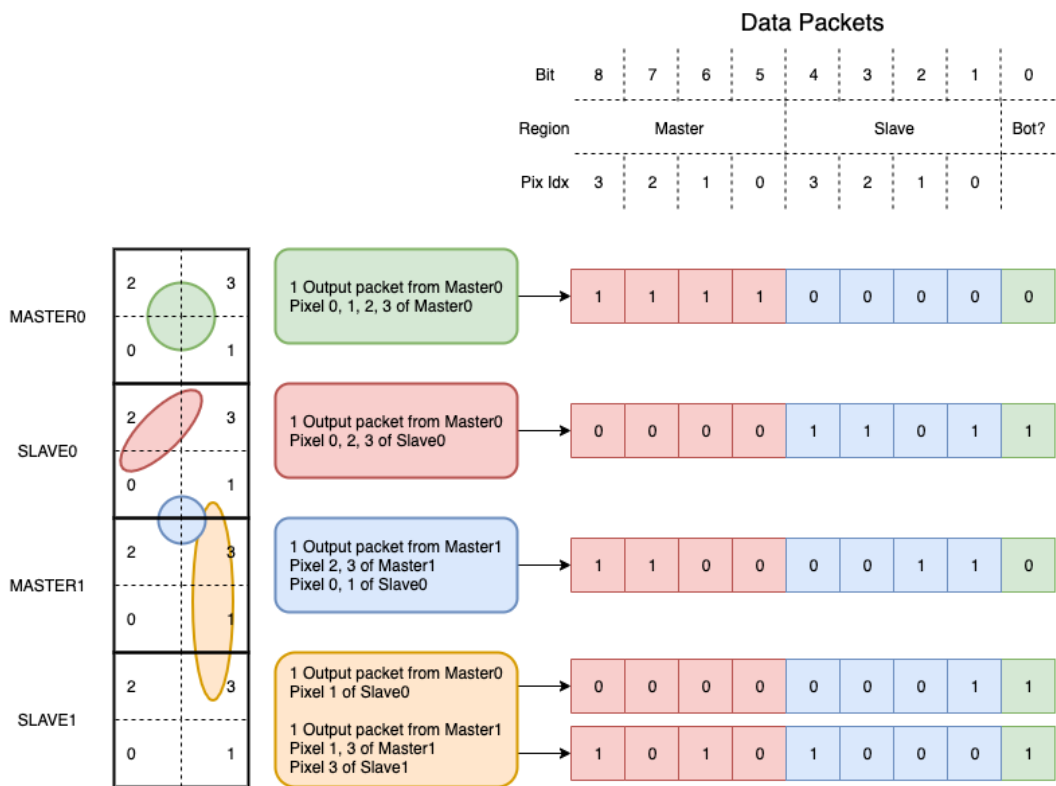


Figure 1.5

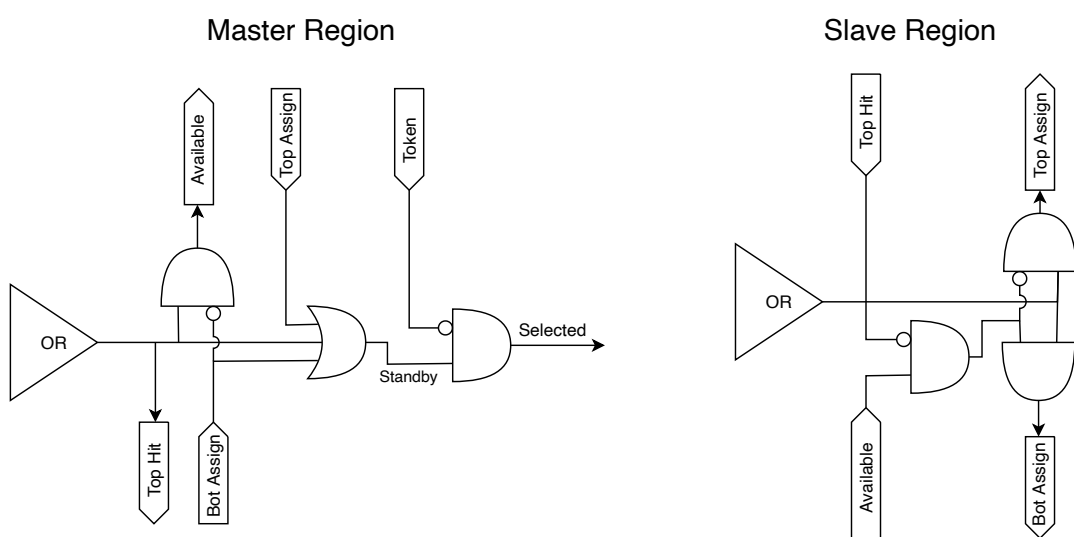


Figure 1.6

94 **Chapter 2**

95 **Characterization**

96

- 97 • rifai il conto della lunghezza di attenuazione. Ho trovato (presentazione Luciano
- 98 Mus) 29 um per ka e 37 um per kb.
- 99 • Con il PMOS la configurazione del FE di default è: e richiama i significati delle
- 100 variabili.

101 **2.1 TJ-Monopix1 characterization**

102 **2.1.1 Threshold and noise: figure of merit for pixel detectors**

103 A characterization of threshold and noise is typically necessary since these values have an
104 impact on the operating conditions and on the performance of the chips, so much that
105 the signal to threshold ratio may be considered as the figure of merit for pixel detectors
106 rather than the signal to noise ratio. The mean minimum stable threshold evolved through
107 different generation of chips: in the 1st generation it was around 2500 e^- while in the 3rd
108 (corresponding to nowadays chips) is less than 500 e^- . This allows in thinner sensors with
109 smaller signals: from $16\,000\text{ e}^-$ produced in $200\text{ }\mu\text{m}$, the signal expected moved down to
110 2000 e^- produced in $25\text{ }\mu\text{m}$. In agreement with this, the threshold of TJ-Monopix1 is
111 around 500 e^- .

112 Obviously the threshold has to be located between the noise peak around the baseline
113 and the signal distribution, in particular it has to be low enough to mantain a high signal
114 efficiency, but also high enough to cut the noise: for a low threshold many pixels can fire
115 at the same time and a positive feedback can set off a chain reaction eventually, causing
116 all the other pixels to fire. Thus, the noise sets a lower bound to the threshold: 117 if an
118 occupancy $\leqslant 10^{-4}$ is required, for example, this correspond to the Gaussian 1-sided tail
119 fraction for 3.7σ . In this case, if the noise is 100 e^- (resonable), the threshold must be
120 higher than $3.7 \times 100\text{ e}^-$. Typically this argument sets only a minimal bound to the
121 threshold since the variation with time and from pixel to pixel have to be taken into
122 account: the temperature, the annealing (for example, the radiation damages in the oxide
123 layer causes shift of MOSFET threshold voltage) and the process parameters variation
124 across the wafer (as for example process mismatch between transistors).

125 On the other hand, concerning the noise, given that the first stage of amplification is
the most crucial, since in the following stages the signal amplitude is high compared to

126 additional noise, it is valued at the preamplifier input node. Then, the noise is parame-
 127 terized as Equivalent Noise Charge (ENC), which is defined as the ratio between the noise
 128 N at the output expressed in Volt and the out voltage signal S produced by 1 e⁻ entering
 129 in the preamplifier:

$$ENC = \frac{N_{out}[V]}{S_{out}[V/e^-]} = \frac{V_{noise}^{RMS}}{G} \quad (2.1)$$

130 with G expressed in V/e⁻; as the gain increases, the noise reduces .

131 Considering the threshold dispersion a requirement for the ENC is:

$$ENC < \sqrt{(T/3.7)^2 - T_{RMS}^2(x) - T_{RMS}^2(t)} \quad (2.2)$$

132 where the T is the threshold set, T_{RMS} is the threshold variation during time (t) and
 133 across the matrix (x); a typical reasonable value often chosen is 5 ENC.

134 Because of the changing of the 'real' threshold, the possibility of changing and adapting
 135 the setting parameters of the FE, both in time and in space is desiderable: these parameters
 136 are usually set by Digital to Analog Converter (DAC) with a number of bit in a typical
 137 range of 3-7. Unfortunately DAC elements require a lot of space that may be not enough
 138 on the pixel area; therefore, the FE parameters are typically global, which means that they
 139 are assigned for the whole chip, or they can be assigned for regions the matrix is divided
 140 into. The former case corresponds to TJ-Monopix1's design in which 7 bits are used for
 141 a total 127-DAC possible values, while the latter corresponds to the ARCADIA-MD1's
 142 one, **where quanti bit??**. An other possibility, for example implemented in TJ-Monopix2,
 143 is allocate the space on each pixel for a subset of bits, then combinig the global threshold
 144 with a fine tuning. If so, the threshold dispersion after tuning is expected to decrease
 145 depening on the number of bits available for tuning:

$$\sigma_{THR,tuned} = \frac{\sigma_{THR}}{2^{nbit}} \quad (2.3)$$

146 where σ_{thr} is the RMS of the threshold spread before tuning.

147 To measure the threshold and noise of pixels a possible way is to make a scan with
 148 different known injected charge: the threshold corresponds to the value where the efficiency
 149 of the signal exceeds the 50%, and the ENC is determined from the slope at this point.
 150 Assuming a gaussian noise, e.g. a noise whose transfer function turns a voltage δ pulse in a
 151 gaussian distribution, the efficiency of detecting the signal and the noise can be described
 152 with the function below:

$$f(x, \mu, \sigma) = \frac{1}{2} \left(1 + erf \left(\frac{x - \mu}{\sigma\sqrt{2}} \right) \right) \quad (2.4)$$

153 where erf is the error function. Referring to 2.4 the threshold and the ENC corresponds
 154 to the μ and σ .

155 I used the injection circuit available on the chip to inject 100 pulses for each input
 156 charge for a fixed threshold. The injection happens on a capacity at the input of the FE
 157 circuit, whose nominal value is 230 aF and from which the conversion factor from DAC
 158 units to electrons can be obtained: for the PMOS flavor, for example, since the DAC are
 159 biased at 1.8 V, the Least significant Bit (LSB) corresponds to a voltage of 14.7 mV from
 160 which the charge for LSB 1.43 e⁻/mV and the conversion factor therefore is 20.3 e⁻/DAC.
 161 While this value is equivalent for all the PMOS flavor, the HV flavor is expected to have a
 162 different conversion factor, ~ 33 e⁻/DAC, beacuse of the different input capacity. Besides

	PMOS A	PMOS B	PMOS C	HV
Threshold [e ⁻]	401.70±0.15	400.78±0.24	539.66±0.58	403.87±0.19
Threshold dispersion [e ⁻]	32.90±0.11	32.97±0.17	55.54±0.42	44.67±0.15
Noise [e ⁻]	13.006±0.064	12.258±0.068	13.88±0.11	11.68±0.10
Noise dispersion [e ⁻]	1.608±0.044	1.504±0.046	1.906±0.072	1.580±0.068

Table 2.1: Mean threshold and noise parameters for all flavor and their dispersion on the matrix.

163 the charge, also the duration and the period of the injection pulse can be set; it is important
 164 to make the duration short enough to have the falling edge during the dead time of the
 165 pixel (in particular during the FREEZE signal) in order to avoid the undershoot, coming
 166 at high input charge, triggering the readout and reading spurious hits. Since the injection
 167 circuit is coupled in AC to the FE, if the falling edge of the pulse is sharp enough to
 168 produce an undershoot, this can be seen as a signal.

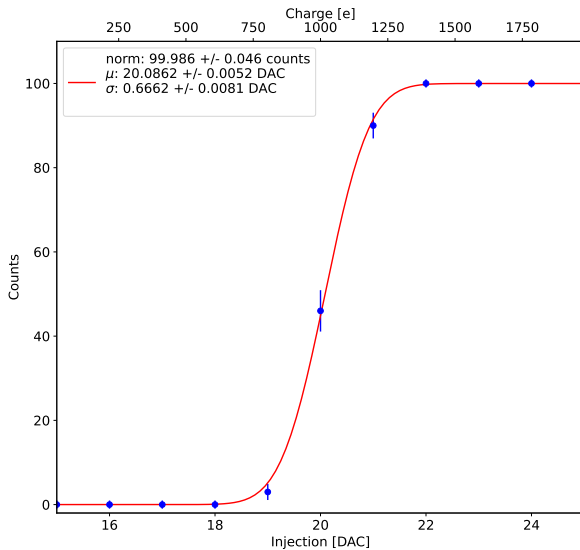


Figure 2.1: S-curve for pixel (10, 10) of the PMOS flavor (flavor 1) with IDB fixed at 40 DAC. The conversion of charge injected from DAC to electrons has been performed using a nominal conversion factor of 20.3 e⁻/DAC

169 with IDB equal to 40 DAC

170 Therefore I fitted the counts detected using the function in equation 2.4. Figure 2.1
 171 shows an example of such fit for a pixel belonging to the flavor B, while in figure 2.2 are
 172 shown the 1D and 2D distributions of the parameters found. I fitted the 1D distributions
 173 with a gaussian function to found the average and RMS of the noise and the threshold for
 174 each flavor across the matrix. The results are reported in table 2.1.

175 In the map at the top right panel of figure 2.2 (IDB=40 DAC) a slightly lower thresh-
 176 old is visible in the first biasing section (columns from 0 to 14); similar structures, but
 177 extended to the entire matrix, appear more evidently when using different IDB values.
 178 The systematic threshold variation across the biasing group has not a known motivation,

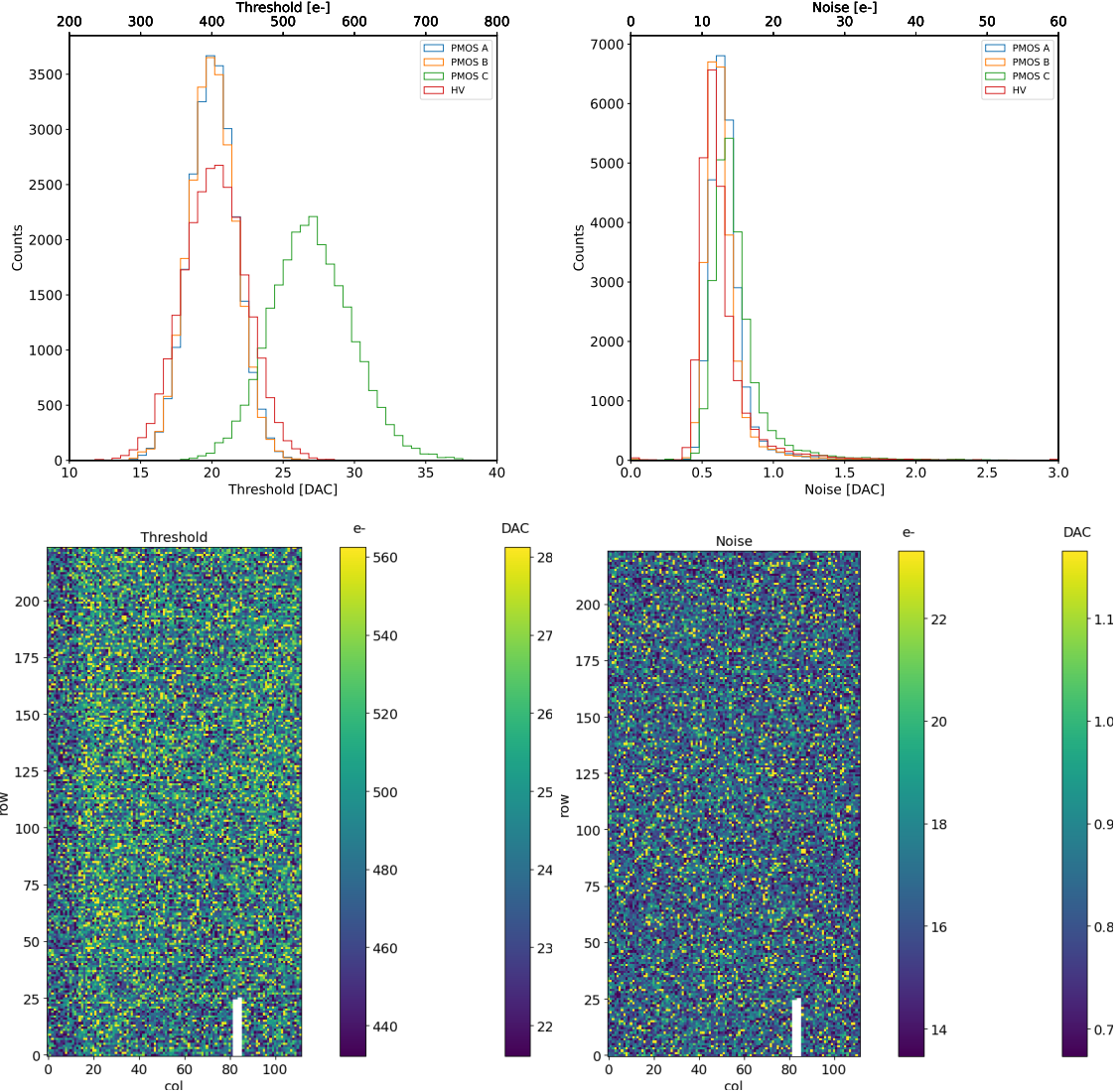


Figure 2.2: Histograms of the threshold (a) and the noise (b) found fitting the s-curve of all flavor with IDB fixed at 40 DAC. Below there are the maps of the threshold (a) and the noise (b), respectively, found fitting the s-curve with IDB fixed at 40 DAC for the PMOS flavor (B). The white pixels have the injection circuit broken.

179 but one could certainly be the transistor mismatch of the biasing DAC registers IDB
 180 and ICASN, which both adjust the effective threshold (I recall that ICASN regulate the
 181 baseline).

182 To verified the trend of the threshold as a function of the front end parameter IDB and
 183 find its dynamic range, I have permormed different scans changing the FE register IDB.
 184 For each IDB I have injected the whole matrix and search for the mean and the standard
 185 deviation of the threshold and noise distributions. The results are shown in figure 2.3:
 186 the blue points are the mean threhsold found whithin the matrix, while in green is shown
 187 the width of the threshold distribution, aka the threshold dispersion. While the threshold
 188 increases, the ENC decreases of ~ 4 e $^-$,which is $\sim 1/3$ of the noise at IDB=40 DAC.

189 Then, to evaluet the operation and the occupancy of the chip at different threshold
 190 I have made long acquisitions of noise at different IDB and check how the number of

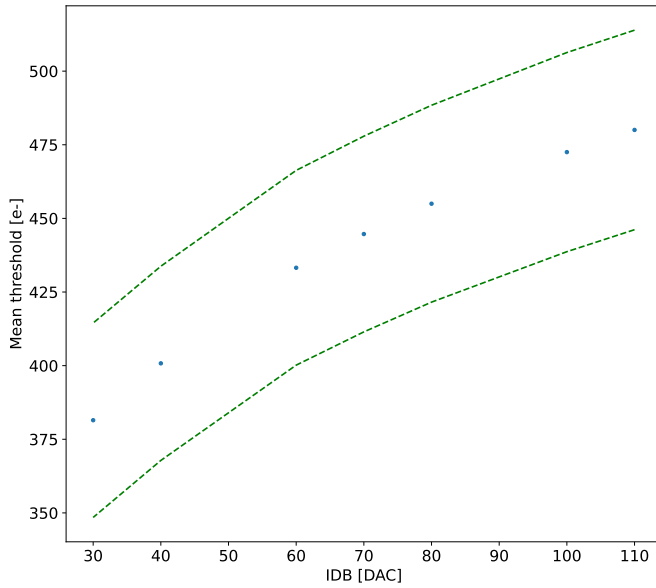


Figure 2.3: Flavor PMOS (B) with Psub-Pwell biased at -6 V. Threshold measured in electrons vs the register which sets the threshold, IDB.

191 pixel masked changes with the threshold. The masking algorithm I have used search for
 192 pixels with rate >10 Hz and mask them. With such algorithm, in our standard condition,
 193 IDB=40 DAC, a very low noise hit rate is intentionally achieved masking a dozen of pixels
 194 of the whole flavor.

195 2.1.2 Linearity of the ToT

196 I have already said in chapter ?? that TJ-Monopix1 returns an output signal proportional
 197 to the charge released by a particle in the epitaxial layer, which is the Time over Threshold;
 198 the ToT is saved as a 6-bit variable and then has a dynamic range equal to 0-64, which
 199 corresponds to 0 μ s to 1.6 μ s assuming a clock frequency of 40 MHz. When a pulse is longer
 200 than 1.6 μ s the counter rolls back to zero and there is no way to distinguish that charge
 201 from a lower one with the same ToT: that is the rollover of the ToT (2.4(a)).

202 In order to associate the ToT (in range 0-64) to the charge, a calibration of the signal
 203 is necessary. Assuming the linearity between ToT and the charge, Q can be found:

$$204 Q[DAC] = \frac{(ToT[au] - offset[au])}{slope[au/DAC]} \quad (2.5)$$

205 where m and q are the fitted parameters of the calibration. It is important to keep in mind
 206 that the main application target of TJ-Monopix1 is in the inner tracker detector of HEP
 207 experiments, then the main feature is the efficiency, then a rough calibration of the signal
 208 to charge is fine. The ToT information can be used both to better reconstruct the charge
 209 deposition in cluster in order to improve the track resolution, and for particle identification,
 especially for low momentum particles which do not reach the proper detectors.

210 The study of the output signal is made possibile via the injection: since the pulses
 211 are triangular, the ToT is expected to be almost therefore, to prevent th linear. To verify

212 this statement and study the deviations from linearity I fitted the ToT versus the charge
 213 injected for all the pixels within the matrix. In figure 2.4(b) there is an example of fit
 214 for a pixel belonging to the flavor B, while in figure 2.5 there are the histograms and the
 215 maps of the parameters of the line-fit for all flavors with IDB fixed at 40 DAC. Here again
 216 a difference among the biasing section appears: since the slope of the ToT is related with
 217 the gain of the preamplifier (increasing the gain also increases the ToT), the mismatch is
 218 probably due to the transistor contributing to the amplification stage.

219 I fitted the average ToT of all the pulses recorded as a function of the pulse amplitude;
 220 data affected by rollover have been removed in order to avoid introducing a bias in the
 221 mean values. In figure 2.4 (b) are shown both the fits with a line (red) and with a second
 222 order polynomial (green): at the bounds of the ToT range values deviate from the line
 223 model. Since the deviation is lower than 1% and it only interests the region near the 0
 224 and the 64, in first approximation it is negligible.

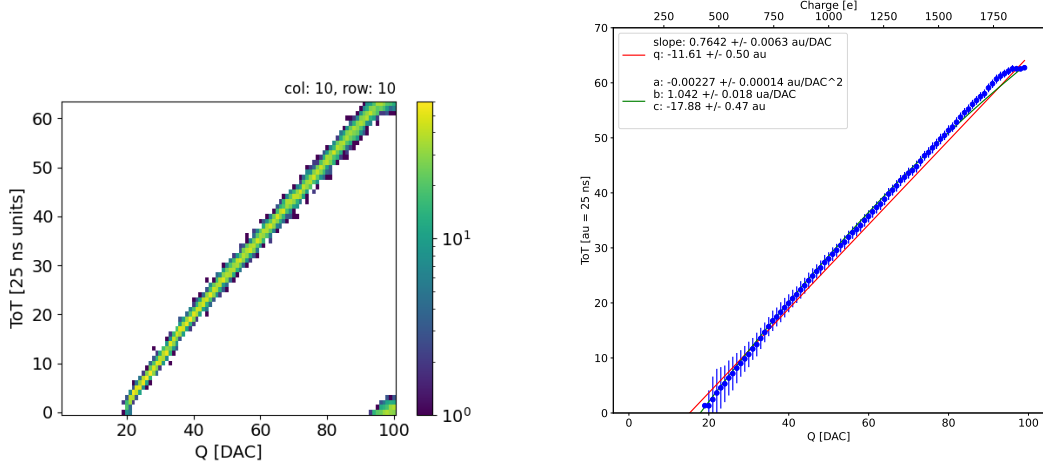


Figure 2.4: The figures refer to pixel (10,10) of the PMOS-reset flavor B with IDB fixed at 40 DAC. (a) Histogram of the injection pulses: the ToT is in range 0-64 since it is represented by 6 bit, so when achieving the 64 it rolls over back to the zero. (b) Mean ToT vs the the charge: the mean has been calculated cutted the rolling hits.

225 2.1.3 Calibration of the ToT

226 Finding a calibration for the ToT means defining a way to pass from the ToT values
 227 (0-64 clock counts) to a spectrum expressed in electrons collected. The principles of the
 228 calibration are the following: the ToT in clock counts maps (eq.2.1.2) a DAC range between
 229 the threshold and a value which depends on the pixel and generally is around 90-100 DAC.
 230 Assuming that a 0 DAC signal corresponds to 0 e⁻, if another reference point is fixed, a
 231 linear calibration function can be defined. After the calibration the ToT goes to map
 232 a charge range between the threshold and Q_{max} which is a function of the pixel and is
 233 around 2 ke⁻.

234 Moreover, considering that the charge injected in the FE goes to fill a capacitor C
 235 which is different from pixel to pixel, the true charge injected does not correspond to what
 236 expected assuming C equal to 230 aF, which is the nominal value. Accordingly to that,
 237 a measurement of this value provides both an absolute calibration of C and a conversion
 238 factor K to have a correspondence of the DAC signal in electrons. K and C are defined

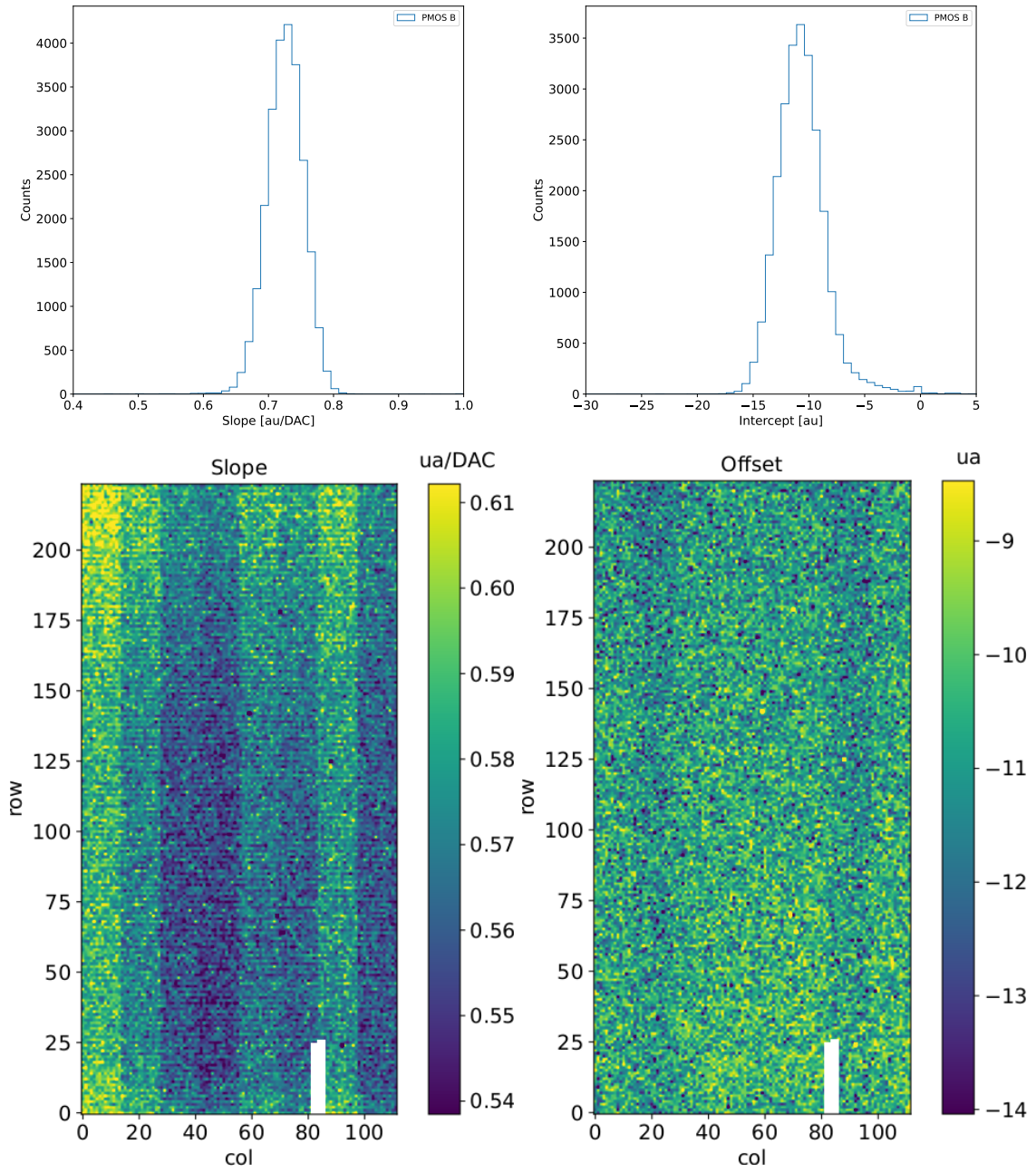


Figure 2.5: Histograms of the calibration parameters, slope (a) and offset (b), found fitting the ToT with a line, for the flavor B and with IDB fixed at 40 DAC. Maps of the calibration parameters, slope (a) and offset (b), found fitting the ToT with a line, with IDB fixed at 40 DAC.

239 respectively as:

$$K [e^- / DAC] = \frac{1616 [e^-]}{Q [DAC]} \quad (2.6)$$

240

$$C [F] = [e^- / DAC] \frac{1.6 \cdot 10^{-19} [C]}{14.7 [mV]} \quad (2.7)$$

241 where K is expected to be $20 e^- / DAC$, assuming the nominal value of C equal to $230 aF$,
242 and where 1616 is the expected number of electrons produced by the calibration source

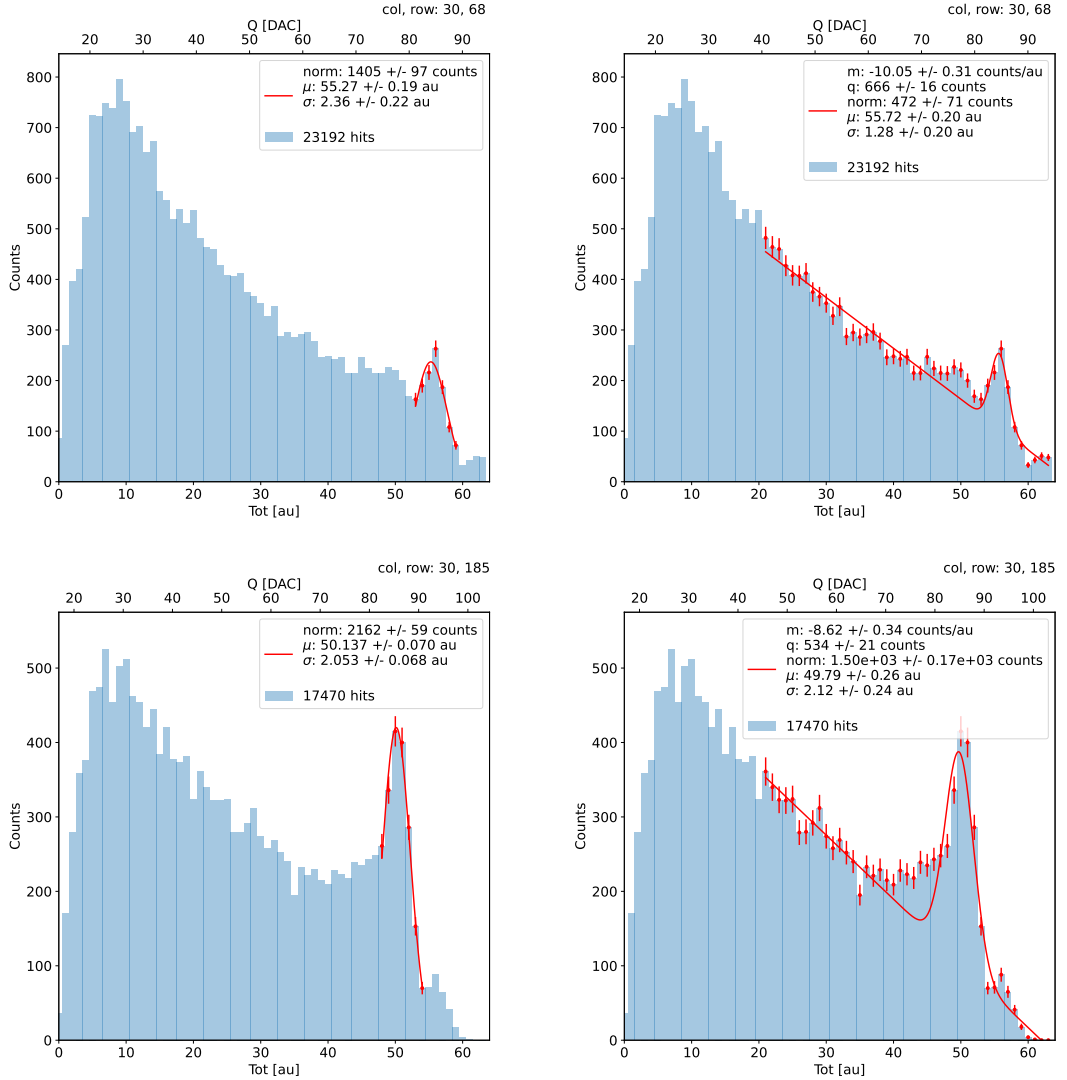


Figure 2.6: due pixel per far vedere la differenza tra i fit. Sottolinea che in rosso ci sono i bin fittati. La doppia scala utilizza le info trovate nel paragrafo precedente per il dato pixel in questione. Per avere una corrispondenza grezza in elettroni basta moltiplicare per 20 e- / dac.

used, Fe55. Fe55 is an extremely important radionuclide in the calibration of X-ray spectrometers, proportional counter and scintillator detector since it emits two X-photons during the electron capture decay: the first one (K_{α}) at 5.9 keV and the second one (K_{β}) at 6.5 keV. The K_{α} photon, which does photoelectric effect in silicon, has an absorption length $\lambda=7 \mu\text{m}$ to $8 \mu\text{m}$, and the probability of being absorbed in the $25 \mu\text{m}$ thick epitaxial layer is $\sim 0.95\%$. The electron emitted has an energy equal to the photon, so recalling that the mean energy needed to produce a couple electron-vacuum is 3.65 eV, the signal produced by the Fe55 source is expected to be 1616 e^- . In figures 2.6 are shown two histograms of the ToT spectrum of the Fe55 source for two different pixels. The peak on the right corresponds to the events with complete absorption of the charge in the depleted region, while the long tail on the left to all the events with partial absorption due to charge sharing among neighbors pixels. In order to reduce the consistent charge sharing, the pixel dimension in TJ-Monopix2 has been reduced down to $30 \times 30 \mu\text{m}^2$. The events on the right

side of the peak, instead, corresponds to the K_β photons. Looking at the histograms for pixel (30, 185) and (30, 69) a significant difference in the peak to tail ratio leaps out, which can be related with the position of the pixel in the matrix. In particular, because of a different charge collection property, pixels in the upper part of the matrix (rows 112-224) have a more prominent peak, while in pixels in the lower part (rows 0-111) there is a higher partial absorption. Indeed, as discussed in section ??, there is a distinction in the structure of the low dose-epi layer among the rows, in particular pixels in rows 112-224, which have a RDPW, are supposed to have a higher efficiency in the pixel corner.

For the calibration I needed to establish the peak position; to do that I fitted the ToT histogram of each pixel. I tested two different fit functions:

$$f(x, N, \mu, \sigma) = \frac{N}{\sigma\sqrt{2\pi}} e^{-\frac{1}{2}(\frac{(x-\mu)}{\sigma})^2} \quad (2.8)$$

266

$$f(x, m, q, N, \mu, \sigma) = m x + q + \frac{N}{\sigma\sqrt{2\pi}} e^{-\frac{1}{2}(\frac{(x-\mu)}{\sigma})^2} \quad (2.9)$$

The additional linear term in equation 2.9 is meant to model the tail due to incomplete

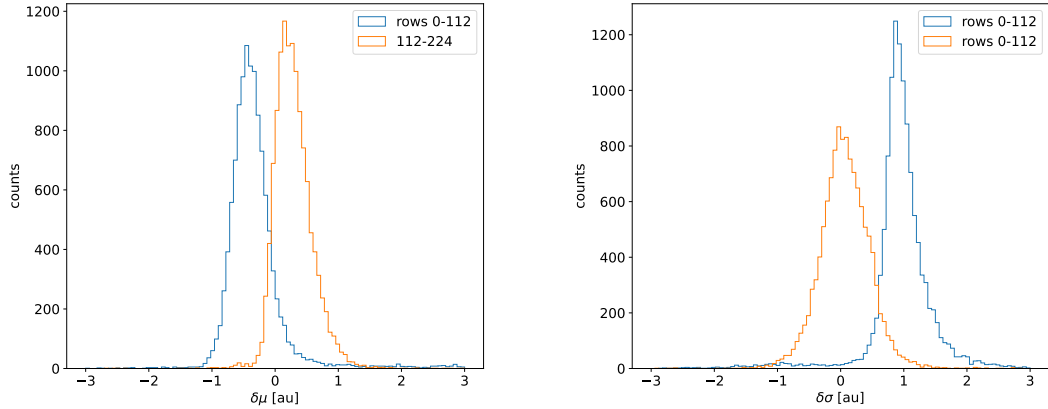


Figure 2.7: Difference between the parameters μ and σ obtained with the gaussian fit and those obtained with a gaussian plus a line. When $\mu < 0$ the fit with function 2.8 is generally worse (the peak is shifted to the left); when $\sigma < 0$, the fit with 2.9 is worse (larger sigma).

267

charge collection and prevent it from introducing a bias in the fitted peak position.

268 For this reason, when fitting with eq.2.9, I selected a larger region compared to the
269 fit with eq.2.8, for which I used only a small reagion around the peak. The optimal fit
270 region was chosen in both cases through an iterative routine: for the fit with eq.2.9 it
271 starts from an interval including all the pixels above 20 DAC and progressively reduces it
272 by increasing the left boundary; for the fit with eq.2.8, it starts from an interval of 5 bins
273 around the expected peak position and reduces the interval of 1 bin at each iteration.

274 Even if the difference in the peak position between the two fit strategies is not really
275 relevant for the purpose of the calibration, being of the order of 0.8-1.5% (2.7),it still
276 introduces a systematic bias towards lower values due to the contribution of the tail.
277 Indeed, we know that the sharp edge on the right must correspond to the case of complete
278 absorption of the photon, so that, in general, the closest to this feature is the fitted peak
279 position, the better the fit is. A poor fit tends also to overestimate the peak width. Even

281 looking at the χ^2 , the fit function 2.8 seems to be the better choice, except for a sample
 282 of pixels in the lower part of the matrix, the one with lower efficiency.

283 The resolution of the detector, which is expected to be determined by the statistical
 284 fluctuations in the number of charge carriers generated in the detector as well as by the
 285 ENC, can be compared to the observed Fe55 peak width. Ideally:

$$\sigma_{Fe} = \sqrt{ENC^2 + F \times N} \quad (2.10)$$

286 Since the number of e/h pairs produced in the sensor is 1616, recalling that F for a silicon
 287 detector is 0.115 and that the ENC measured with the injection is 12e- , the σ_{Fe} is
 288 expected to be $\sim 18\text{e-}$. Looking at figure 2.8 the resolution achieved with the Fe55 source
 289 seems to be much higher. A contribution we have not taken into account but is certainly
 290 relevant is the systematic overestimation of the standard deviation of the Fe55 peak: this,
 291 as I already explained, is principally due to the high background of incomplete charge
 292 collection, which broadens the fitted peak.

293 2D maps of the value of the capacity and of the conversion factor found are shown in
 294 2.9. The evident stripe-structure in the matrix shows an evident correlation among the
 295 same row; the same structure, which is also visible in the slope map of the calibration of
 the ToT (fig.??), may be related with the structure of the bias lines.

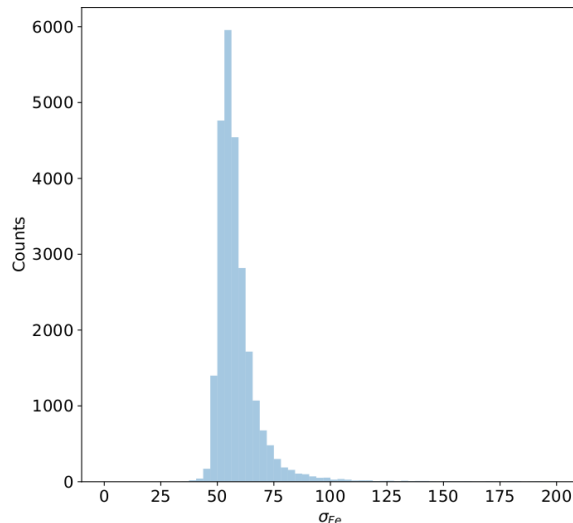


Figure 2.8: Distribution of the Fe55 peak width.

296

297 HV flavor calibration

298 An attempt of calibrating the HV flavor, which is the most different from the PMOS B
 299 flavor, has been performed; however, because of the loss of signal caused by the higher
 300 capacity, we have been unable to identify the Fe55 peak in every FE and bias configuration.
 301 An example of Fe55 spectrum collected with the HV flavor is shown in figure 2.10.

302 2.1.4 Changing the bias

303 In order to study the behavior of the sensor as a function of the bias, I performed several
 304 injection scans in different configurations. Indeed, the thickness of the depletion region has
 305 to be considered an important parameters affecting the signal efficiency, and in particular

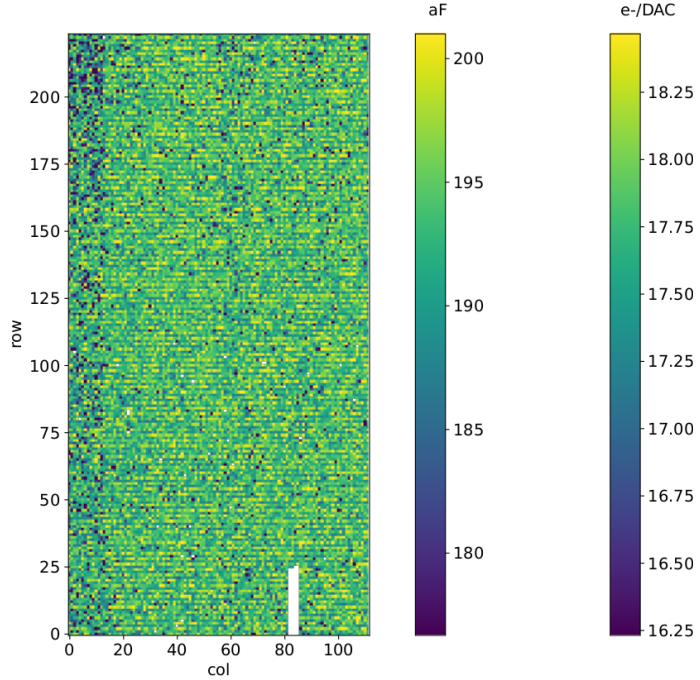


Figure 2.9: Map of the capacity (calibrated) at the input of the injection circuit.

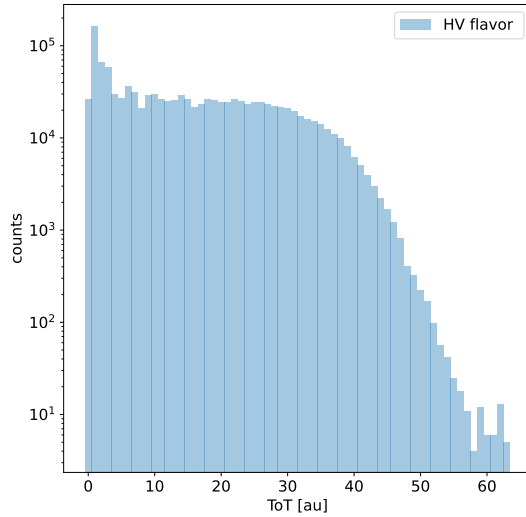


Figure 2.10: Fe55 spectrum with the HV flavor

it affects the charge released by a particle which crosses the sensor (since the signal is proportional to the thickness of the epitaxial layer). The measured output voltage amplitude and gain in the case of the PMOS and HV flavours are shown in figure 2.11 Given that the chip under examination has a gap in the low dose epi-layer, we were not able to change independently the bias of the substrate (PSUB) and of the p-well (PWELL), but they must be kept at the same value, differently from other chips of the same submission. Lowering the bias, the depletion region is expected to narrow and the efficiency to reduce, especially in the pixel corner, thus raising the threshold and the noise and decreasing the slope as a consequence of the reduction in the gain.

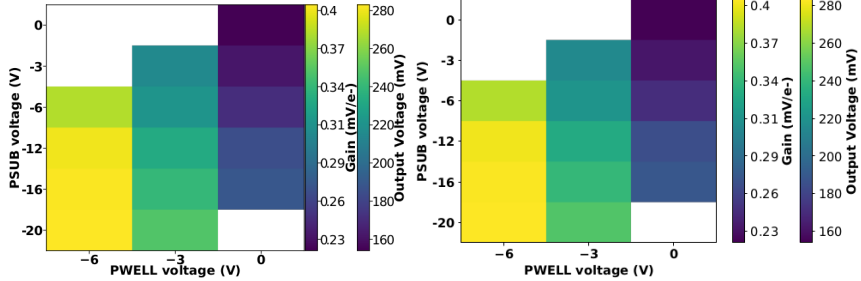


Figure 2.11: Output voltage amplitude and gain with respect to the p-well and p-substrate voltage in the case of the PMOS reset front-end (B)

	-6 V	-3 V	0 V
Threshold [DAC]	20.0 ± 1.6	21.0 ± 1.6	24.5 ± 1.8
Noise [DAC]	0.613 ± 0.075	0.625 ± 0.078	0.822 ± 0.098
Slope [au/DAC]	0.726 ± 0.027	0.707 ± 0.028	0.573 ± 0.021
Offset [au]	-10.8 ± 1.9	-11.2 ± 1.8	-11.1 ± 1.5

Table 2.2: The errors are the standard deviations of the corresponding distributions. The conversion factor from DAC to electrons is $\sim 20 \text{ e}^-/\text{DAC}$.

315 In order to test the behavior of the chip when not completely depleted, I have performed
 316 an injection scan with PSUB/PWELL bias at 0 V, -3 V and -6 V (results in tab.2.2), and
 317 some acquisitions with the Fe55 source (fig. 2.12). There are reported the values of the
 318 K_α peak position, the normalization of the events above the peak and the rate, everything
 319 has been normalized to the value at the reference condition, which is with PSUB/PWELL
 320 at -6 V.

321 2.1.5 Measurements with radioactive sources

322 In order to completely validate the operation of the whole sensor¹, I have performed several
 323 acquisitions with radioactive sources, specifically Fe55 and Sr90Y, which is a β^- emettitor
 324 with electron endpoint at 2.2 MeV, and cosmic rays. I used the data collected with Sr90
 325 and cosmic rays, to study charge sharing and events with more than one hit.

326 I define *cluster* the ensamble of all the hits with the same timestamp. This is obviously
 327 a coarse requirement, but it gave me the opportunity of using a simple and fast clustering
 328 algorithm, which is fine when the random coincidence probability is negligible. Defining
 329 R_1 and R_2 as the two events rate, and τ as the dead time of the detector, the random
 330 coincidence rate can be found:

$$R_{coinc} = R_1 \times R_2 \times \tau \quad (2.11)$$

331 As I am going to prove in the next section, the dead time strictly depends on the occupancy
 332 of the matrix, even though we can assume a dead time of $\sim 1 \mu\text{m}$, which corresponds to
 333 the mean dead time per pixel. However, if in an event a particle hits two different pixels
 334 producing a cluster, the total dead time simply doubles. Since the measured rate on the

¹As I will discuss in chapter 3.2 these measurements serves also as a reference for the spectrum observed at the test beam

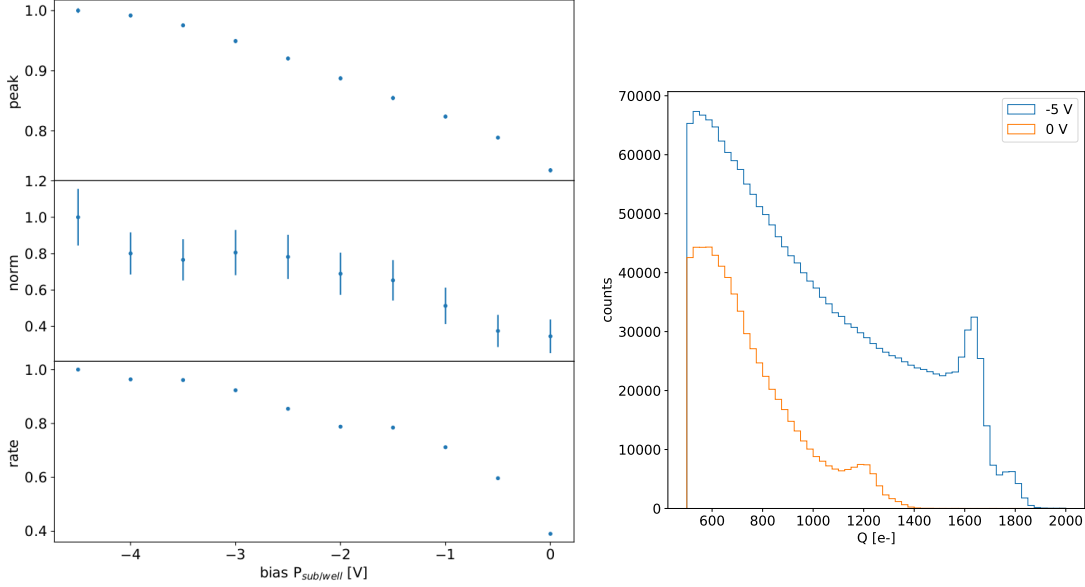


Figure 2.12: (a) Peak position, peak amplitude and rate as a function of the bias. Since during the collection of the whole data the source has been moved, it is not guaranteed that it has always had a repositioning in the same exactly place, then small the fluctuation of the rate along the decreasing trend are acceptable. The peak position and amplitude are estimated by fitting the spectrum with a gaussian in the region around the peak. (b) Fe55 spectrum at different $P_{sub/well}$ bias. The ToT values have been calibrated as explained in section.

2.1.3.

whole matrix of noise, Fe55, Sr90 and cosmic rays are \sim Hz, 3.3 kHz, 40 Hz and \sim 10 mHz², the random coincidence probability are negligible except the one of two Fe55 events, which is 11 Hz.

In figure 2.13 I report the histograms of the number of pixels in the cluster and of the dimension of clusters, defined in terms of the max and min coordinates on the matrix as:

$$d = \sqrt{(y_{max} - y_{min})^2 + (x_{max} - x_{min})^2} \quad (2.12)$$

Looking at the shape of the histogram of the dimension, generally the Sr90 and the cosmic rays produce bigger clusters and hit a higher number of pixels, a trend that can be explained considering that the Fe55 photoelectron is much less energetic than the Sr90 electron and cosmic rays. Below I have also attached a sample of hitmap of events produced by the three different sources (fig.2.14, 2.15).

In figures 2.17 are shown the distributions per different cluster dimension events, of the charge collected by a single pixel (figures on the left) and the charge collected by summing all the pixels in the cluster (on the right). In order to remove the background, since the rate noise rate is comparable with the ones of cosmic rays and Sr90, in the plots I have cut the single pixel events. **DISEGNO** The charge per length covered Q/l released by a particle which crosses more pixels and is not completely absorbed in the sensor (fig.??) can be described by the following relation. Considering that:

$$l = \frac{t}{\cos(\lambda)} = \frac{t}{\sqrt{1 + tg^2 \lambda}} = \frac{t}{\sqrt{1 + (x/t)^2}} \quad (2.13)$$

²The cosmic rays rate at the sea level is expected to be \sim 1/cm²/s

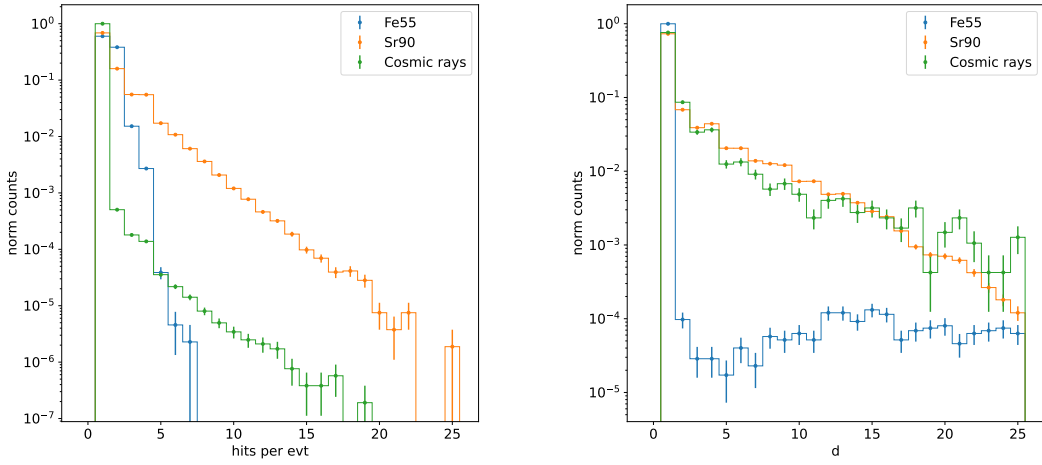


Figure 2.13: (a) Distribution of the number of hits per event with different sources. (b) Dimension of cluster defined as eq.2.1.5. Compared with the Sr90 and the cosmic rays, the Fe55 d distribution is characterized by a clear discontinuity in the cluster dimension. The very thin peak around 0 corresponds to the effective cluster, while the long tail at bigger cluster d is principally made of random coincidence.

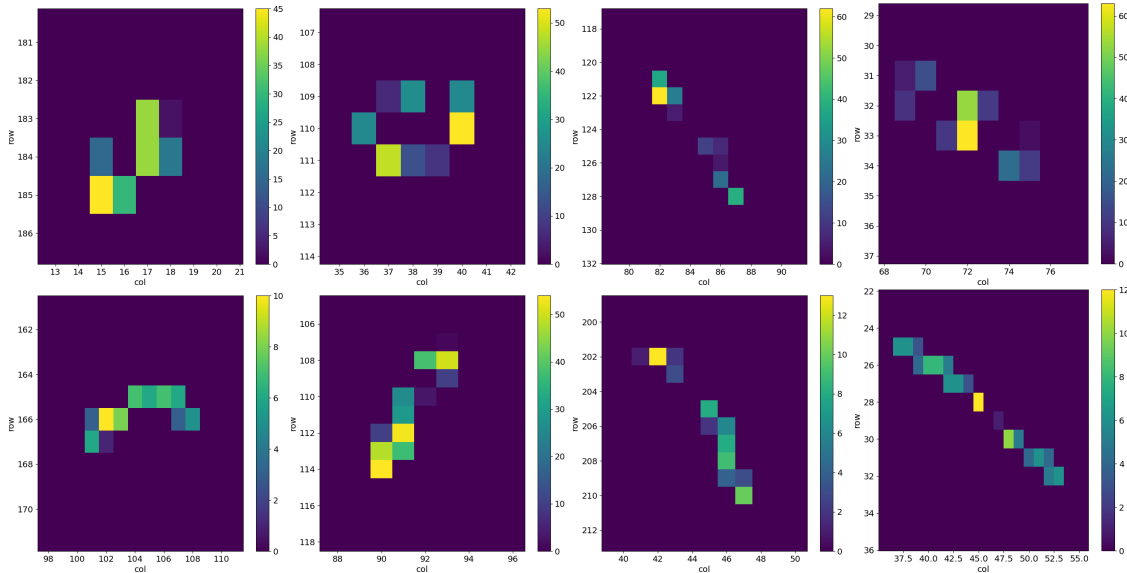


Figure 2.14: 2D histograms of the ToT in different events in an acquisition of cosmic rays.

352 it can be expressed as:

$$\frac{Q}{l} = \frac{Q}{t} \sqrt{1 + (n - 1)^2 p^2 / t^2} \quad (2.14)$$

353 where p/t is the ratio between the pitch and the epitaxial layer thickness, and then it is
 354 different in the x and y directions ($40 \mu\text{m}$ and $36 \mu\text{m}$ respectively). Taking as value of p/t
 355 1.52, which is the mean on the two axis, the value of Q/l expected by the scaling relation
 356 and the charge actually measured in the acquisition with the Sr90 are illustrated in table
 357 2.3; because of the decision of cutting the single pixel events in order to have a clean
 358 sample, the expected value has been obtained by the two hits cluster dividing the charge

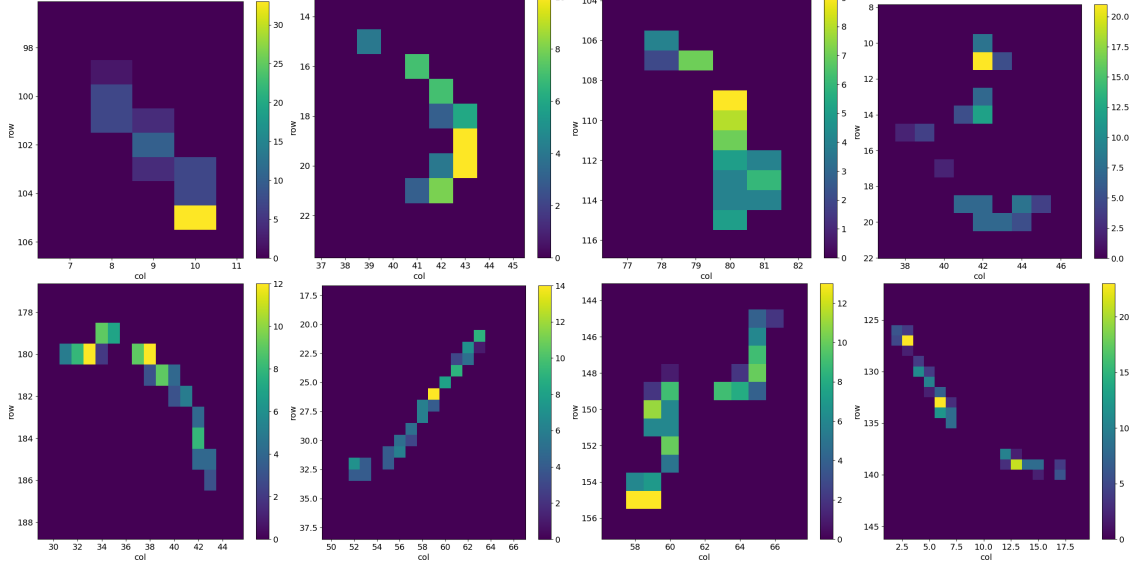


Figure 2.15: 2D histograms of the ToT in different events in an aquistion of Sr90.

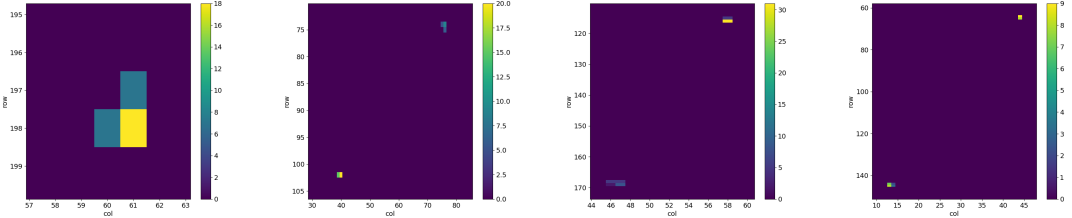


Figure 2.16: 2D histograms of the ToT in different events in an aquistion of Fe55

359 by 2. The single pixel charge is then expected to be **conto**. The measured value has been
360 obtained by the maximum of the distributions in the left plots in 2.17

361 **Bump a sinistra dei cosmici?** Per quanto riguarda il ferro mi sarei aspettata che
362 sommando la carica nel cluster la somma rimanesse sempre a 1616. Questo è verificato
363 abbastanza bene da cluster con 2 e 3 hits, invece 4 ha il picco a 1850, questo significa
364 probabilmente che quando hai 4 hit hai sia un fotone che un hit di rumore con basso tot,
365 e che quindi ha carica circa la soglia. Guardando invece allo spettro di signolo pixel si
366 vede per i clyster da 2 e 3 un piccolo bump a 1600. Probabilmente questo corrisponde a
367 eventi di ferro in cui una delle due hit ha tutta la carica e l'altra invece è un evento di
368 rumore. 3. Invece 4 ha il picco a 1850, questo significa probabilmente che quando hai 4
369 hit hai sia un fotone che un hit di rumore con basso tot, e che quindi ha carica circa la

Pixel per evt	Expected [e-]	Measured [e-]
2		950 ± 30
3		1450 ± 30
4		2050 ± 30
5		2450 ± 30

Table 2.3: Scaling proved with the events coming from the Sr90

370 soglia. Guardando invece allo spettro di signolo pixel si vede per i clyster da 2 e 3 un
 371 piccolo bump a 1600. Probabilmente questo corrisponde a eventi di ferro in cui una delle
 372 due hit ha tutta la carica e l'altra invece è un evento di rumore.

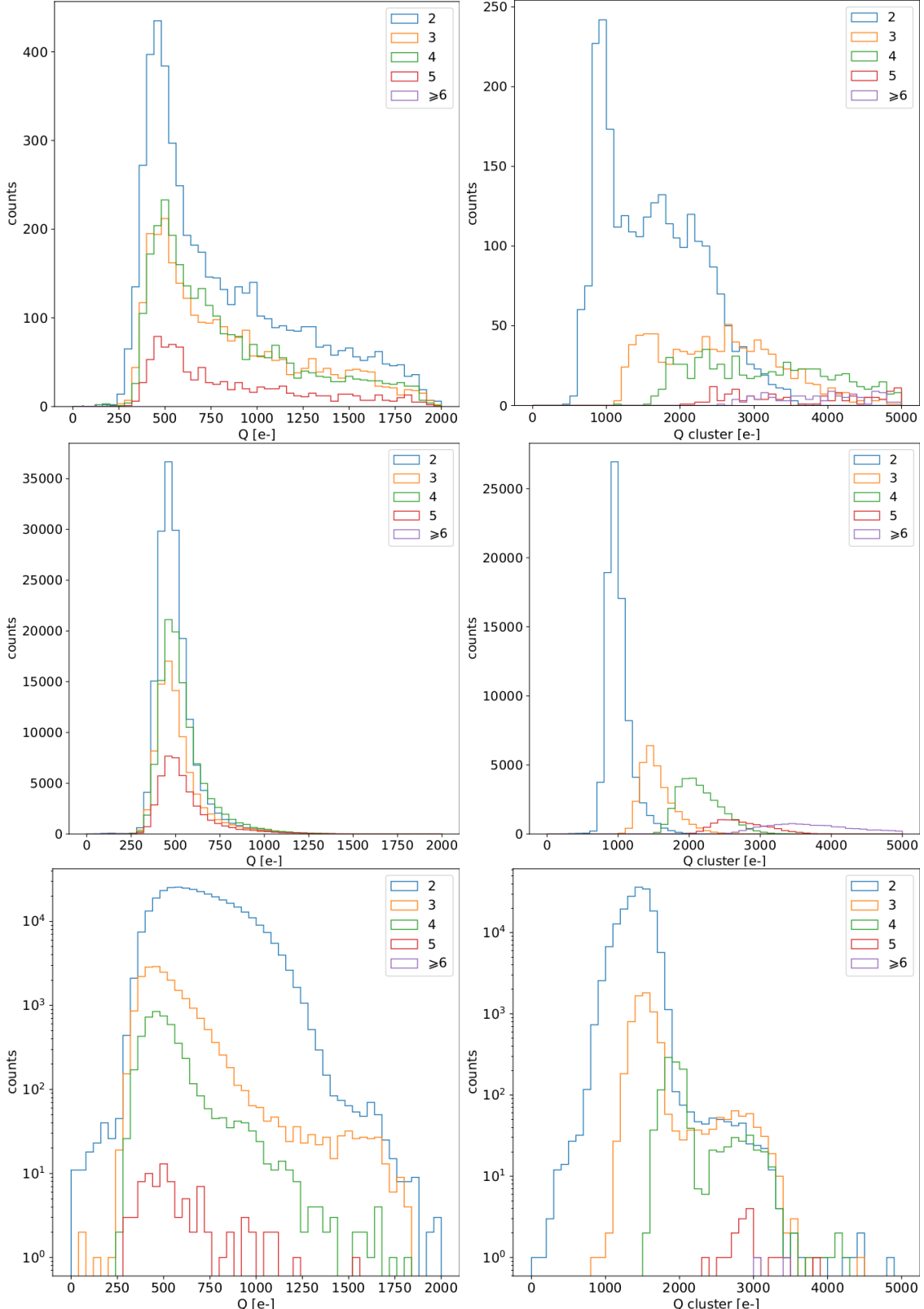


Figure 2.17: Acquisitions with radioactive source and cosmic rays at IDB=40 DAC.

373 spiegazione cosmici.

374 **2.1.6 Dead time measurements**

375 The hit loss is due to analog and digital pile up: the first one occurs when a new hit
376 arrives during the pre-amplifier response, the second instead when the hit arrives while
377 the information of the previous hit has not yet been transferred to the periphery. Since the
378 pre-amplifier response has a characteristic time \sim ToT, the dead time τ_a introduced by it
379 will be at most 1.6 μ s; using the IRESET and VRESET FE parameters the reset time can
380 be lowered down, but as explained in section ?? it must be longer than the preamplifier
381 characteristics time in order to not cut the signal. Regarding the latter contribution instead,
382 since only one hit at a time can be stored on the pixel's RAM, until the data have completed
383 the path to get out, the pixel is paralyzed. Moreover since there is no storage memory
384 included on TJ-Monopix1 prototypes, the digital dead time τ_d almost corresponds to the
385 time needed to transmit the data-packets off-chip.

386 The exportation of data from pixel to the EoC occurs via a 21-bits data bus, therefore
387 only one clock cycle is needed and the dead time bottleneck is rather given by the
388 bandwidth of the serializer which transmits data off-chip from the EoC. In our setup the
389 serializer operates at 40 MHz, thus to transmit a data packet (27-bit considering the ad-
390 dition of 6 bits to identify the double-column at the EoC) at least 675 ns are needed. For
391 what we have said so far, the R/O is completely sequential and therefore is expected a
392 linear dependence of the reading time on the number of pixels to read:

$$\tau = 25 \text{ ns} \times (\alpha N + \beta) \quad (2.15)$$

393 where α and β are parameters dependent on the readout chain setting.

394 To test the linearity of the reading time with the number of pixels firing and to measure
395 it, I have used the injection circuit which allows me choosing a specific hit rate: I made
396 a scan injecting a fix number of pulses and each time changing the number of pixels
397 injected. Indeed the injection mode allows fixing not only the amplitude of the pulse,
398 which corresponds to the charge in DAC units, but also the time between two consecutive
399 pulses (DELAY). The hit rate then corresponds to 25 ns/DELAY.

400 Unfortunately a high random hit rate on the matrix cannot be simulated by the in-
401 jection because of the long time (\sim ms) needed to set the pixel registers of the injection;
402 then I was forced to specify at the start of the acquisition the pixels to inject on, and for
403 convenience I chose those on a same column. In figure 2.18 is shown the dependence of
404 the efficiency on the DELAY parameter in two different cases. For the 5 pixels example
405 the efficiency goes down the 90% at a DELAY of \sim 185 clock counts, which corresponds
406 to 4.625 μ s and to a rate of 216 kHz, while in the 10 pixels example, the efficiency goes
407 under the 100% at \sim 380 clock counts, which corresponds to 9.5 μ s and to a rate of 105 kHz.
408 From the efficiency curves I have then looked for the time when the efficiency decreases.
409 In figure 2.19(a) is shown the dead time per pixels as a function of N with different R/O
410 parameters configuration, the meaning of which is explained in chapter ???. The default
411 value suggested by the designer of the chip are reported in table 2.4; moving too much
412 the readout parameters from the default ones, the readout does not work properly, and no
413 hits can be read at all. The problem probably stays in the firmware setting of the readout
414 which are specially fixed for our chip **Sul repository, nei commenti ci sono altri valori pos-**
415 **sibili per il FREEZE, ma avevamo detto che probabilmente sono relativi ai setting di altri**

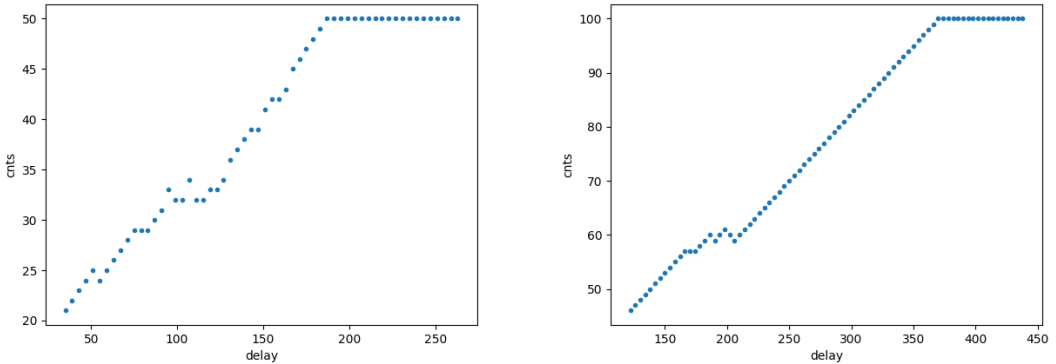


Figure 2.18: Efficiency vs the DELAY parameters. (a) I made a scan injecting 5 pixels with 50 pulses for each DELAY configuration and (b) 10 pixels with 100 pulses for each DELAY

Parameter	Value [DAC]	Value [μ s]
START_FREEZE	64	1.6
STOP_FREEZE	100	2.5
START_READ	66	1.65
STOP_READ	68	1.7

Table 2.4: Default configuration of the R/O parameters

416 **chip.** Despite the single pixel reading time does not depend on the position on the pixel
 417 matrix, whithin a clock count which is ~ 25 ns, and it is equal to 106 clock counts, since
 418 the τ_d critically depends on the pixel position on the matrix: in particular the reading
 419 sequence goes from row 224 to row 0, and from column 0 to column 112, making the pixel
 420 on the bottom right corner the one with the longest dead time.

421 Furthermore to test that there is no dependence of the digital readout time from the
 422 charge of the pulse, I have try to change the amplitude of the pulse injected, but the
 423 parameters found were consistent with the default configuration ones. No difference in
 424 the α and β coefficients has been observed between the two case. Referring to eq.2.15, the
 425 factor α is proportional to the difference (STOP_FREEZE - START_READ), while the
 426 offset β lies between 5 and 15 clock counts.

427 The readout time found by this test is so long because in the prototypes no paralleliza-
 428 tion of the informations (with the instroduction of more serializer for example) and no
 429 storage memory are included; this feature are typically added in the final prototypes. An
 430 example closely linked to TJ-Monopix1 is OBELIX: it will include on the chip a storage
 431 buffer to optimize the dead time and to keep a low occupancy even at high fluence.

432 2.2 ARCADIA-MD1 characterization

433 Unfortunatly the characterization of MD1 has not yet been completed because of some
 434 problems with the functionality of the first chip we received on which we have been able
 435 to make only a few electrical and communication test in order to test the operations of the
 436 FPGA and the breakout board (BB). We asked for another chip then but we, due to

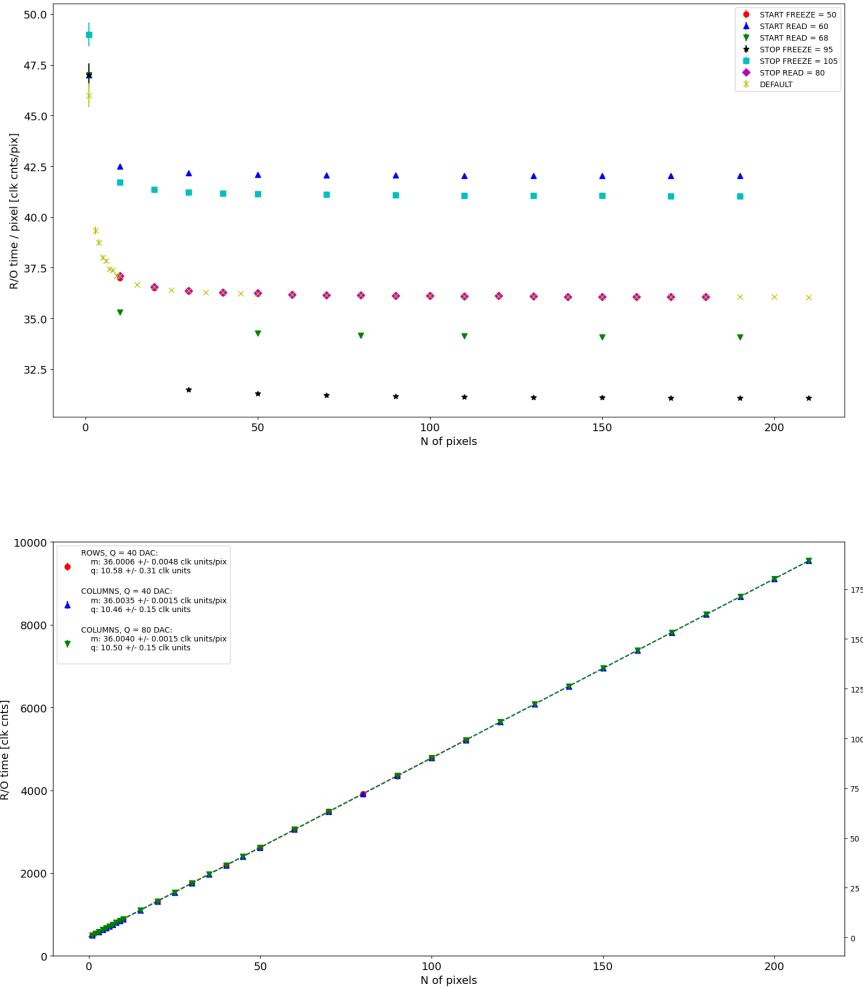


Figure 2.19: (a) Readout time per pixel as a function of the number of pixel injected obtained with different FE setup. (b) Readout time as a function of the number of pixels injected obtained injecting pulses with amplitude of 80 DAC (green), of 40 DAC on the same row (red) and on the same column (blue).

delay in the extraction and the bonding of the wafer, have received it one week ago; an exhaustive characterization and testing of the new chip have been going on in the clean room on the INFN, and I am going to show here only some preliminary results.

The problem with the broken chip occurs when it is biased, in particular, when the HV voltage is lowered down 0V, the sensor requires too much power and a too high current draw sets. We have discussed the problem with the designers of the chip whose helped us identifying the motivation of the break: the chip has been glued using too much conductive tape and hence have a short-circuit between the sides and the back, which makes impossible the biasing. Unfortunately, since both the sensor and the FE require at least -10 V to work properly, no measurement was possible except the acquisition of the noise in the FE circuit.

The second chip we received is a minid2, that is a "mini demonstrator" from the second submission. The two have the same characteristics but the minid2 is smaller than the MD1, in particular it only have 32×512 pixels, instead of 512×512 .

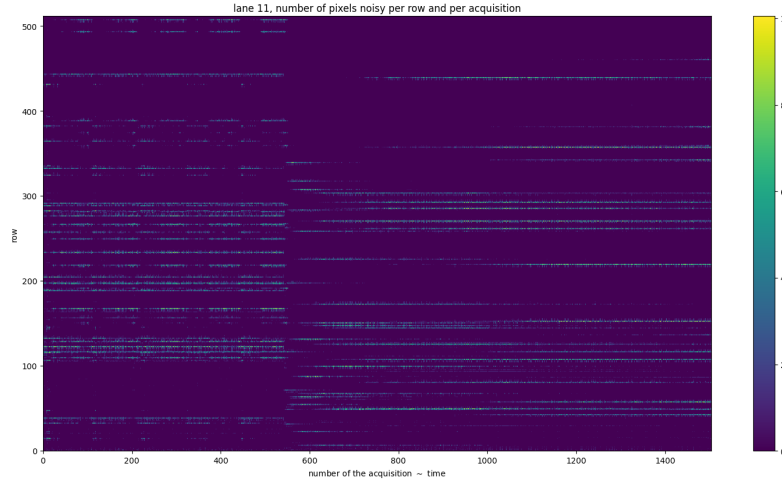


Figure 2.20: Noise in the front end circuit depending on the bias road across the matrix was recorded.

451 Up to now we used the injection circuit in order to make a threshold scan on a few
 452 pixels: differently from the TJ-Monopix1's characterization where we performed a scan
 453 changing the injection charge of the pulse, with the minid2 we have instead changed the
 454 threshold (whose register is VCASN) keeping the charge of the pulse fixed. For each
 455 threshold we inject 100 pulses of amplitude 10 μ s. The dependence of the efficiency on the
 456 threshold for two pixels is shown in figure 2.21. Even if the behavior is reasonable, as the
 457 threshold is reduced the efficiency becomes higher, it is possible that the bias (-50 V) is
 not enough to fully deplete the sensor, since the counts do not reach the 100% steadily.

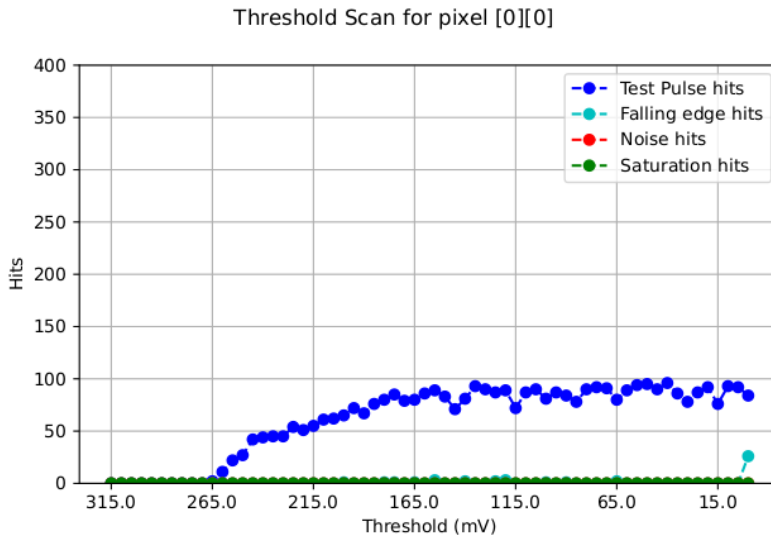


Figure 2.21: Threshold scan on the pixel (0,0). The sensor is polarized with $\Delta V = -50$ V.

458
 459 The value of the SNR and the ENC Charge injection circuit uses $C_{inj} = 2.325$ fF. The
 460 SNR, the ENC and the threshold dispersion on the matrix are expected to be respectively
 461 ~ 90 , $3 e^-$ and $\sim 35 e^-$ with a detector capacity of 7 fF, that is about the capacity expected
 462 for the detector. The injection capacity is expected to be ~ 2.325 fF, and in this condition

463 the the minimum and maximum signals generated are respectively 0.08 fC and 2.6 fC.
 464 Substantial differences have been observed with VCASN=40 DAC in both the efficiency
 465 and the threshold among the sections; this suggests that with this particular FE config-
 466 uration there is a big threshold dispersion on the matrix. The hitmap of an acquisition
 467 with the Fe55 source is shown in figure 2.22: the whole MD1 matrix with only the bottom
 468 region (32 rows) working is represented in (a), while in (b) there is a zoomed hitmap. The
 469 rate seen within the region 8 (green region in the figure (a)) is compatible with the rate
 of the same radioactive source measured with TJ-Monopix1, that it \sim 3.3 kHz. Looking to

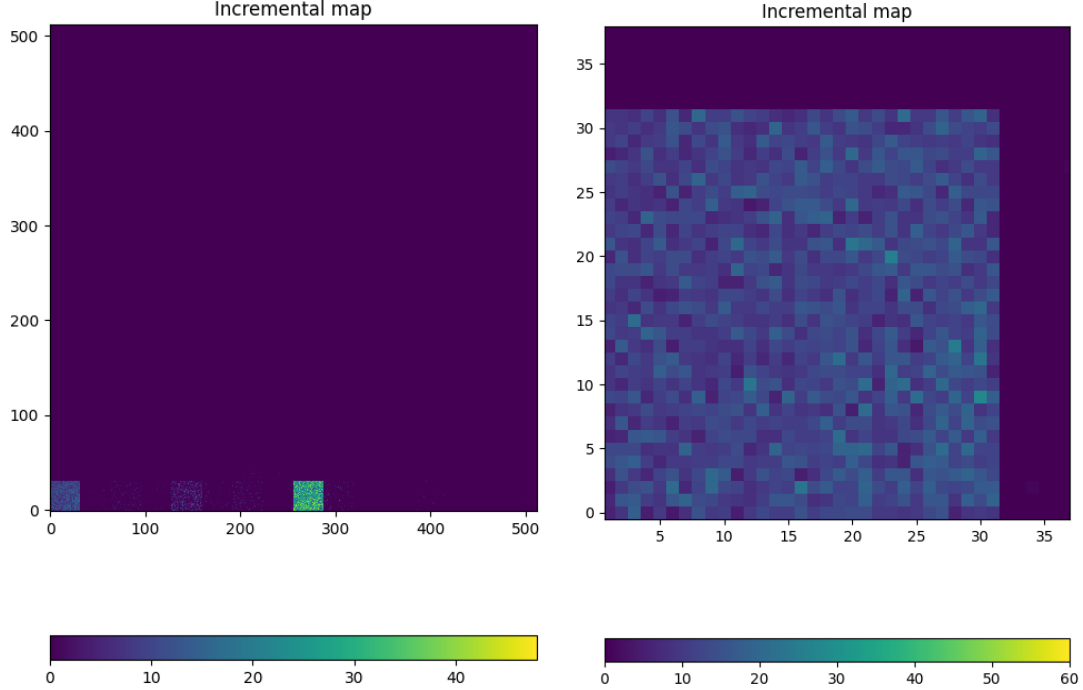


Figure 2.22: Fe55 acquisition with VCASN=40 DAC. (a) All the matrix 512×512 is plotted even if the minid2 has only the rows in range 0-32. (b) A zoom on the first section (col 0-32).

470
 471 the Sr90 acquisitions (fig.2.23) many clusters and tracks can be immidiately distiguished,
 472 confirming what observed with TJ-Monopix1.

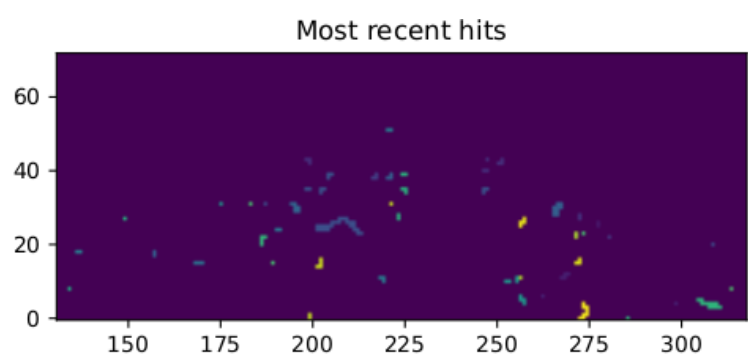


Figure 2.23: Sr90 acquisition with VCASN=40 DAC. The different colours are related with the time of arrival of the hits: in yellow the most recent hits, while in blue the old ones.

⁴⁷³ **Chapter 3**

⁴⁷⁴ **Test beam measurements**

⁴⁷⁵ During August 2022 a testbeam took place in Santa Chiara hospital in Pisa, where a
⁴⁷⁶ new accelerator designed for both medical research and R&D on FLASH-RT, and for this
⁴⁷⁷ reason called "ElectronFlash", have been installed a few months ago. The motivation
⁴⁷⁸ of the testbeam measurements were testing TJ-Mopopix1 at high dose rate with a focus
⁴⁷⁹ on investigating the possibility of the application in radiotherapy. Despite this particular
⁴⁸⁰ device does not seem fitting the requirements imposed for that application, especially
⁴⁸¹ regarding the readout time, the measurements have been useful since help us characterizing
⁴⁸² the setup for future advance, and also give us the possibility of a complete characterization
⁴⁸³ of the chip.

⁴⁸⁴ Given that in medical physics the dose is the standard parameter to characterize the
⁴⁸⁵ beam, because of its obvious relation with the damage caused in the patient, I am going
⁴⁸⁶ to explain the meaning of it by the point of view of the instrumentation. Infact, when
⁴⁸⁷ interacting with measuring systems a more common and useful parameter is the rate or
⁴⁸⁸ the fluence of particles. The conversion between the two quantity can be found thinking to
⁴⁸⁹ the definition of dose: it is the concentration of energy deposited in tissue as a result of an
⁴⁹⁰ exposure to ionizing radiation. Assuming total absorption of electrons in water, defined
⁴⁹¹ by law as the ordinary reference medium, the dose can be expressed as:

$$D[Gy] = \frac{NE[eV]}{\rho[g/cm^3]A[cm^2]x[cm]} \quad (3.1)$$

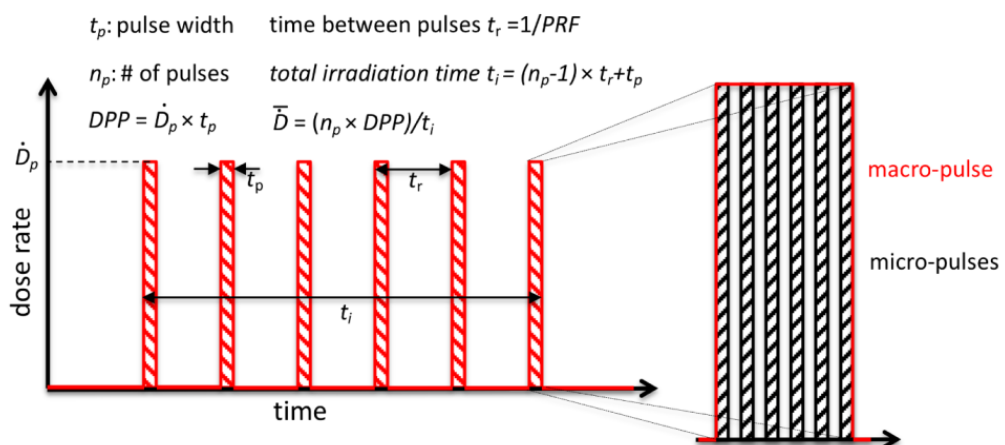


Figure 3.1: Typical beam structure of a beam used in electron radiotherapy

\bar{D}	Dose rate (mean dose rate for a multi-pulse delivery)	0.005-10000 Gy/s
\dot{D}	Intra pulse dose rate (dose rate in a single pulse)	0.01-1 10^6 Gy/s
DDP	Dose in a single pulse	0.04-40 Gy
PRF	Pulse repetition frequency	1-350 Hz
t_p	Pulse width	0.2-4 μ s
n	Number of pulses	single/pulse train

Table 3.1: The parameters that can actually be set by the control unit are the PRF, DDP, t_p and n (in particular the modality of singular irradiation or pulse train), while the other changes consequently.

492 After having applied the conversion of the energy from eV to J and noticed that $E/\rho x$
 493 roughly corresponds to the stopping power S of electrons in water, a simple estimation of
 494 the dose released in water is:

$$D[Gy] = 1.602 \cdot 10^{-10} N[cm^{-2}] S[MeV cm^2/g] \quad (3.2)$$

495 3.1 Apparatus description

496 In order to shield the outdoor from ionizing radiation the accelerator is placed in a bunker
 497 inside the hospital. The bunker has very thick walls of cementum and both the control
 498 units of the accelerator and of the detector were placed outside in a neighbor room.

499 3.1.1 Accelerator

500 The ElectronFlash accelerator is an electron Linear Accelerator (LINAC) with two energy
 501 configurations, at 7 MeV and 9 MeV, and it can reach ultra high intensity (40 Gy/pulse)
 502 keeping the possibility of accessing many different beam parameters and changing them
 503 independently from each other, a characteristic that makes it almost unique worldwide
 504 and which is fundamental for research in FLASH-RT, both for the medical aspects¹ and
 505 for the studies on detectors. The accelerator implements the standard beam structure
 506 used in RT with electrons (fig. 3.1), that is a macro pulse divided in many micropulses;
 507 the parameters used to set the dose and their range of values settable by the control unit
 508 is reported in table 3.1.

509 The accelerator is also provided of a set of triod cannons ~ 1.2 m long and with diameters
 510 in range from 1 cm to 12 cm and a collimator that can be used as beam shaper to
 511 produce a squircle shape. The triode, which is made by plexiglass, must be fix to the gun
 512 during the irradiation and is needed for producing, via the scattering of electrons with it,
 513 an uniform dose profile (fig.3.2) which is desired for medical purpose.

514 3.1.2 Mechanical carriers

515 The tested detector consists in one chip, the Device Under Test (DUT), mounted on
 516 a board and connected to FPGA with same arrangement of figure ???. These boards
 517 have been positioned vertically in front of the triode on a table specifically built for the

¹For example, it is not yet really clear the dependence of the efficacy of the FLASH effect on the whole beam parameters

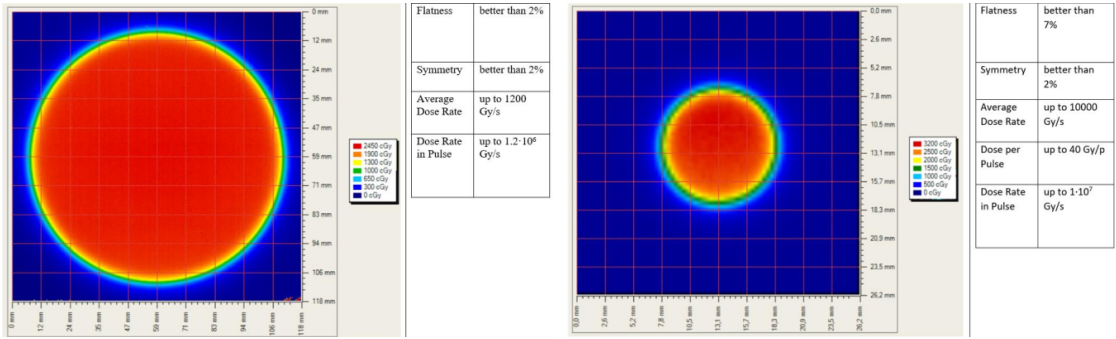


Figure 3.2: Two example of x-y isodose curves for two different triodes, 10 cm and 1 cm respectively, reported by the producer in the manual with the specific of the accelerator (S.I.T. - Sordina IORT Technologies S.p.A.). With the smaller collimator the dose rate in pulse is comparatively higher.

518 testbeam. The tree board have been enclosed in a box of alluminium with a window on
 519 the DUT and with the required holes at the side to enable the biasing via cables and the
 520 connection with the DAQ provided via ethernet cable. A trigger signal coming from the
 521 control unity and syncronized with the pulses emitted from the beam has been also sent to
 522 the FPGA. This digital signal cannot be considered a real trigger, since the TJ-Monopix1
 523 prototype has been designed to be triggerless, but its Time of Arrival (ToA) had allowed
 524 the reconstruction of the correct timing during the analysis.

525 In order to shield the sensor from the whole particles emitted from the gun, two
 526 alluminium collimators have been fabricated: one has been positioned at the triode exit
 527 while the other in front of the DUT. The collimators are $t=32$ mm thick and have a
 528 diameter d equal to 1 mm: assuming a beam divergence bigger than $d/t=1/32 = 1.8^\circ$,
 529 which is the case, the collimator at the triode output was supposed to work as a point
 530 source and to reduce the rate on the DUT of a factor at least $4 \cdot 10^{-4}$. The second one,
 531 being near the DUT, was instead supposed to shield the sensor from the electrons which
 532 have passed the first one, except for a region of 1 mm^2 configurable using *come si chiamano*
 533 *quei cacciavitini per settare la posizione? sliding trimmer?*.

534 3.2 Measurements

535 Because of the dead time of TJ-Monopix1 it is not possible resolving the bunch sub-
 536 structure and almost no one pixel can read more than a hit per bunch. I recall, indeed,
 537 that the dead time per pixel depends on the location on the readout priority chain and
 538 for each pixel $\lesssim 1 \mu\text{s}$ are needed; therefore, assuming a pulse duration of $4 \mu\text{s}$, only a few
 539 pixels at the top of the priority chain (placed at the upper left on the matrix) can fire a
 540 second time, as they can be read a first time before the end of the pulse and then can be
 541 hit again.

542 Since resolving the single electron track is impossible, a way this sensor could be used
 543 in such context is reducing its efficiency and taking advantage of the analog pile up and
 544 of the linearity of the analog output (ToT), in order to see a signal produced not by the
 545 single particle but by more electrons. Reducing the efficiency and the sensibility of the
 546 sensor is essential in order to decrease the high charge signal produced in the epitaxial
 547 layer and mitigating the saturation limit: the smaller the output signal produced by a

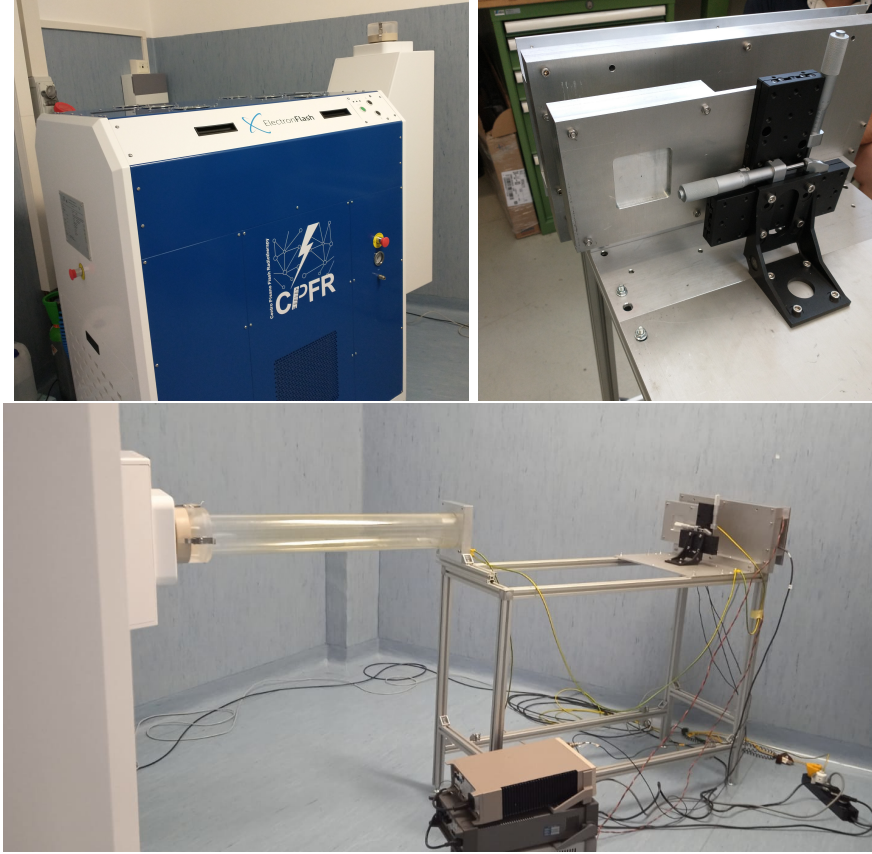


Figure 3.3: Experimental set up. (a) ElectronFlash accelerator: a rotating gantry allows the gun orientation from 0° to 90° (horizontal /vertical). (b) Collimator and DUT box. (c) Whole structure mounted: we used the 10 cm diameter and 1.2 m long triode; the DUT which is in the box behind the two collimators is connected to the power supply units.

548 particle and the higher the fluence the detector can cope with. There is an obvious limit in
 549 this context that is the ToT rollover, indeed, the signal stop giving information when this
 550 value has been overridden and is no more bijective. With the standard configuration of
 551 the FE parameters and the epitaxial layer completely depleted, a MIP produces a charge
 552 at the limit of representation with a 6-bit ToT; to obtain smaller output signals one can
 553 operate on the reduction of the gain.

554 Recalling the results in section 2.1.4, I have shown that concerning the PMOS flavor
 555 B, reducing the bias from -6 V to 0 V brings a reduction of efficiency down to 40 %, and a
 556 reduction in the gain of a factor $\sim 1/3$, while the reduction of the gain of the preamplifier
 557 allows a reduction of **circa 10, ma da controllare**.

558 In order to take advantage of the analog pile up and integrating the charge, for
 559 simplicity assume of two electrons, the second one must hit the pixel before the ToT goes
 560 under the threshold. The general condition is then $\overline{\Delta T} < \overline{ToT}$, but if a high $P_\mu(n \geq 1)$ is
 561 required, a lower $\overline{\Delta T}$ may be desired:

$$P(n \geq 1) = \sum_{n=1}^{\infty} \frac{e^{-\mu} \mu^n}{n!} = 1 - P(0) = 1 - e^{-\mu} \quad (3.3)$$

562

$$\mu = \frac{\overline{ToT}}{\overline{\Delta T}} \quad (3.4)$$

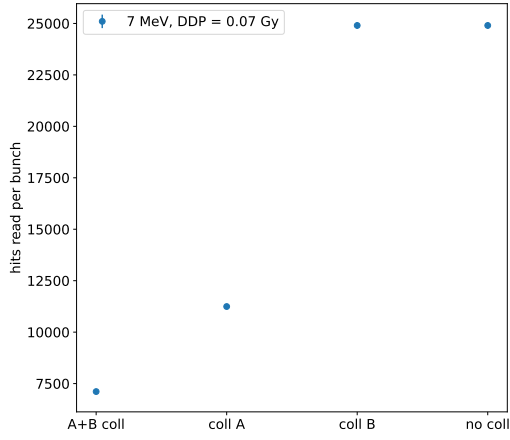


Figure 3.4: Mean number of hits read per bunch at DDP=0.07 Gy, with all the possible setup condition: with both the collimator, with only the collimator far from the chip (A), with only the collimator near the chip (B), and without any collimator.

563 If a $P_\mu(n \geq 1) = 99\%$ then the $\overline{\Delta T}$ must be $\sim 0.22 \overline{ToT}$. The ToT is in range [0,64] but
 564 since the rollover must be avoided, the \overline{ToT} must be lower than 32, and then the minimum
 565 rate on the pixel must be 1.25 MHz.

566
 567 During the testbeam many runs have been performed, spanning the energy, the dose
 568 per pulse and the four possible configurations with/without the collimators. We have
 569 collected data with the PMOS flavor A in the standard configuration: with the PWELL
 570 and PSUB biased at -6 V and set the standard default FE parameters reported in table
 571 ???. During all the data acquisitions we have selected on the control unit of the accelerator
 572 pulses with t_p of 4 μ m and with the smallest PRF settable, which is 1 Hz, in order to start
 573 in the most conservative working point excluding the digital pile up of events from different
 574 bunches. In these conditions, even if the whole matrix turns on, the total readout time
 575 corresponds to $25000 \times 1 \mu s = 25 \text{ ms}$ is still lower than the time between two consecutive
 576 pulses. In figure 3.4 is shown the mean number of hits read during one accelerator pulse
 577 in different setup conditions.

578 The readout starts with the trailing edge of the first pulse going down the threshold:
 579 about 50 clk=1.25 μ s after this moment the FREEZE signal is sent to the whole matrix,
 580 and the transmission of the data to the EoC begins. The hits read during the FREEZE
 581 signal are the ones whose TE occurred before the start of the FREEZE and which have the
 582 TOKEN signal high; the ones, instead, whose TE occur during the FREEZE are stored in
 583 the pixel memory until the end of the FREEZE. At this point a second readout starts and
 584 a second FREEZE is sent to the matrix. An example of the two sub-pulses corresponding
 585 to an electron bunch is shown in figure 3.5: in the acquisition we injected 5 pulses with
 586 both the collimators mounted on the table. Looking at the spectrum we can see that the
 587 second sub-pulse has a populated tail on the right; this is due to the fact that the hits
 588 which arrive before the start of the first FREEZE but have a long ToT that falls during
 589 the FREEZE, are read at the second sub-pulse.

590 The 2D histograms in figure 3.5, reveal an important characteristics of our setup: in

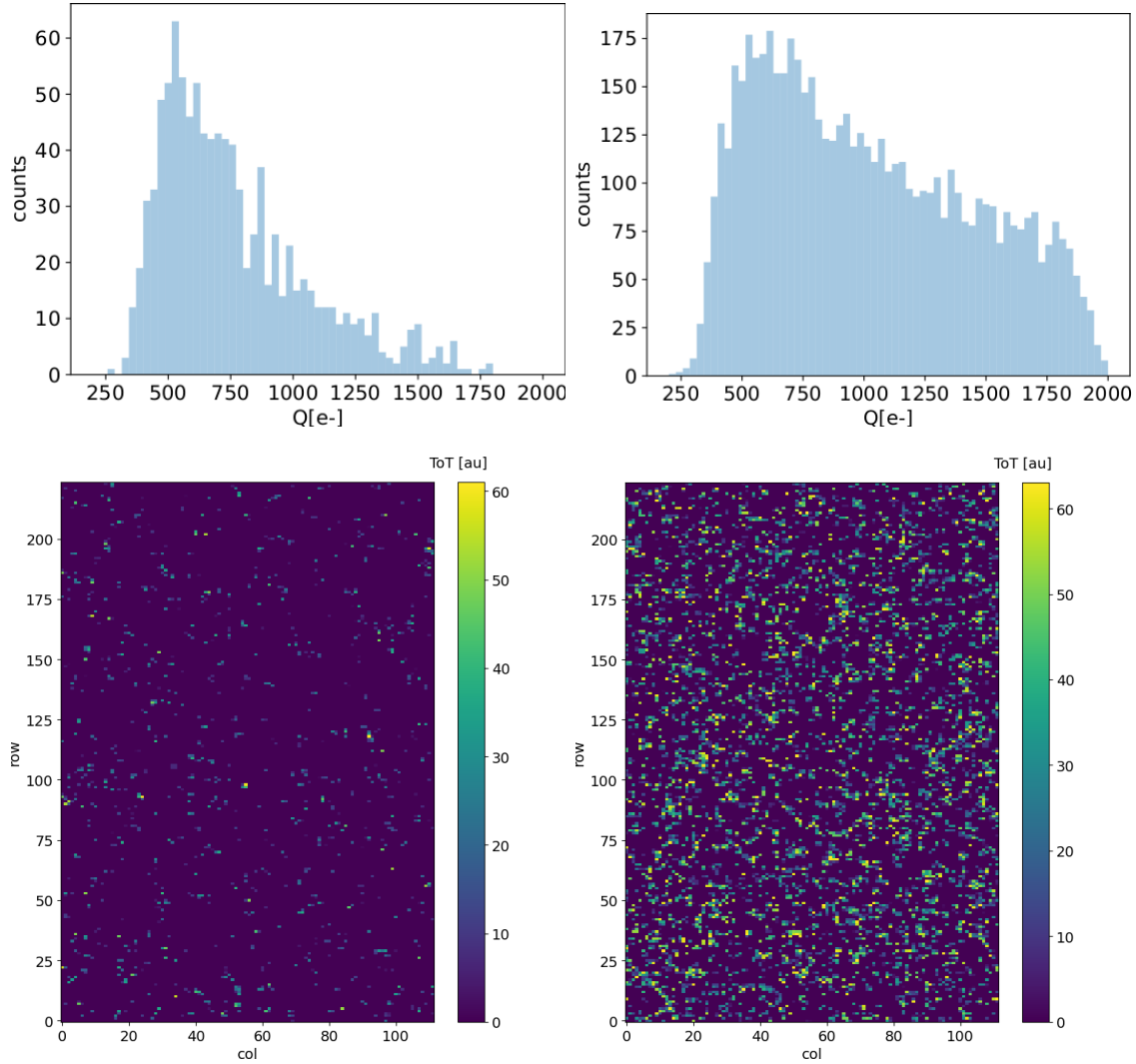


Figure 3.5: Acquisition with both the collimators: 5 pulses at $DDP=0.07\text{ Gy}$. (a) Spectrum of the charge released in the sensor: to apply the conversion I used the information found in the previous chapter. (b) 2D histogram of the ToT of the hits arrived in the sub-pulses.

fact, being uniform and not showing disomogenities, it follows that the collimators do not shield all the particles. We supposed that this was due to a Bremsstrahlung photon background higher than expected but a full verification of that and the analysis of the data is still going on. In figure 3.6, instead, the histograms with a higher DDP value is shown; in the example the matrix turns on completely, but again this happens in two different consecutive read chain.

When we have put aside the collimators, instead, the fluence increase a lot and the two-pulses substructure no more appears (fig. 3.7), but, because of the high attivity of the matrix, after each readout new hits with a fixed ToT were induced due to crosstalk. This problem had already been observed on other prototypes of TJ-Monopix1, and thanks to a simulation it has been observed that the main source of crosstalk is the voltage drop of the pre-amplifier ground as a result of the accumulated current that is drawn from the discriminator.

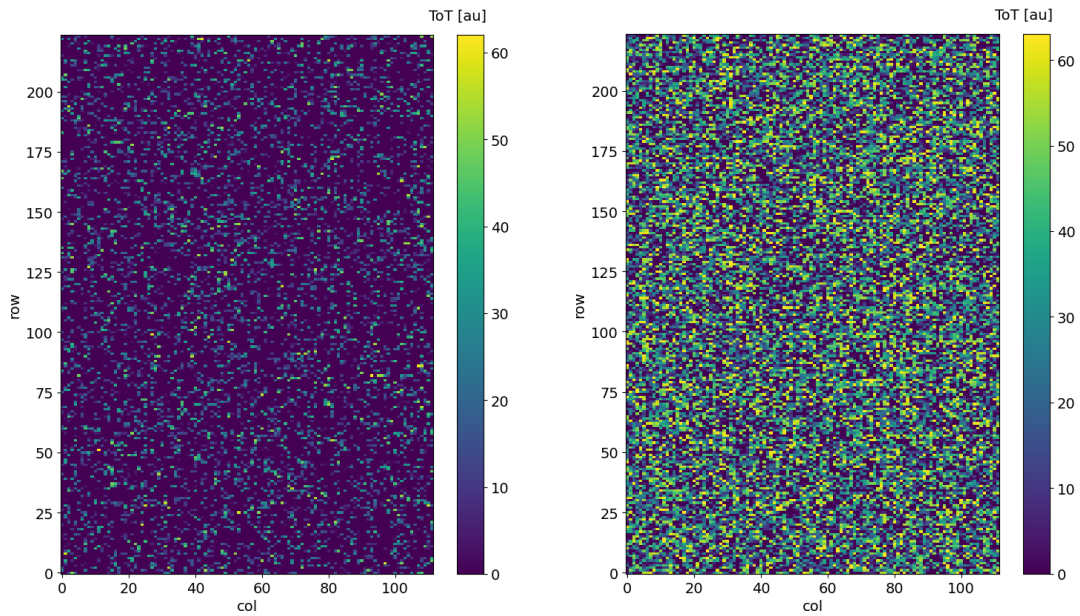


Figure 3.6: Acquisition with both the collimators: 5 pulses at $DDP=0.6\text{ Gy}$. 2D histogram of the ToT of the hits arrived in the sub-pulses. Compared with the previous maps, since the DDP is much higher, more pixels turn on.

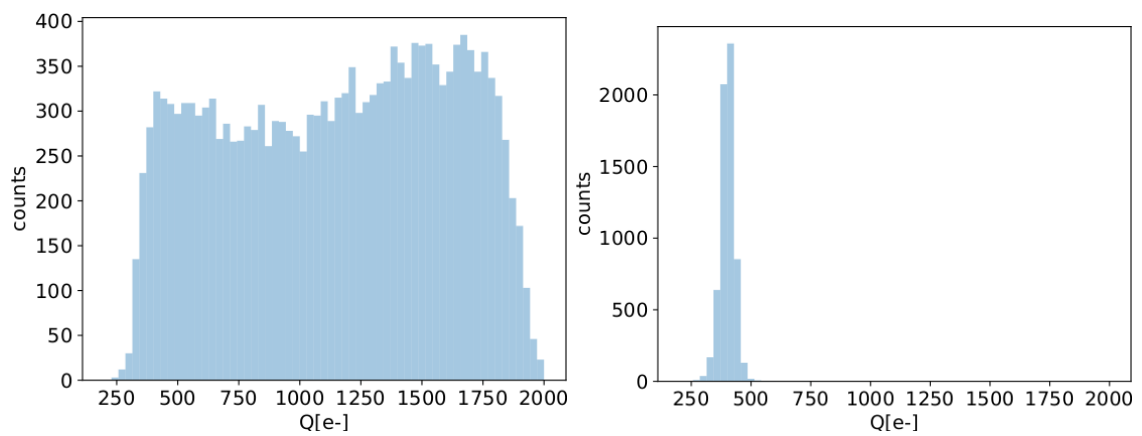


Figure 3.7: Acquisition without any collimator: 5 pulses at $DDP=0.04\text{ Gy}$.

604 Bibliography

- 605 [1] W. Snoeys et al. “A process modification for CMOS monolithic active pixel sensors
606 for enhanced depletion, timing performance and radiation tolerance”. In: (2017).
607 DOI: <https://doi.org/10.1016/j.nima.2017.07.046>.
- 608 [2] H. Kolanoski and N. Wermes. *Particle Detectors: Fundamentals and Applications*.
609 OXFORD University Press, 2020. ISBN: 9780198520115.
- 610 [3] E. Mandelli. “Digital Column Readout Architecture for 10.1109/NSSMIC.2009.5402399
611 the ATLAS Pixel 0.25 um Front End IC”. In: (2002).
- 612 [4] M. Garcia-Sciveres and N. Wermes. “A review of advances in pixel detectors for
613 experiments with high rate and radiation”. In: (2018). DOI: <https://doi.org/10.1088/1361-6633/aab064>.
- 615 [5] C. Marinas. “The Belle-II DEPFET pixel detector: A step forward in vertexing in the
616 superKEKB flavour factory”. In: (2011). DOI: [doi:10.1016/j.nima.2010.12.116](https://doi.org/10.1016/j.nima.2010.12.116).
- 617 [6] J. Baudot. “First Test Results Of MIMOSA-26, A Fast CMOS Sensor With Inte-
618 grated Zero Suppression And Digitized Output”. In: (2010). DOI: [doi:10.1109/NSSMIC.2009.5402399](https://doi.org/10.1109/NSSMIC.2009.5402399).
- 620 [7] A. Dorokhov. “High resistivity CMOS pixel sensors and their application to the
621 STAR PXL detector”. In: (2011). DOI: [doi:10.1016/j.nima.2010.12.112](https://doi.org/10.1016/j.nima.2010.12.112).
- 622 [8] Giacomo Contin. “The STAR MAPS-based PiXeL detector”. In: (2018). DOI: <https://doi.org/10.1016/j.nima.2018.03.003>.
- 624 [9] Nolan Esplen. “Physics and biology of ultrahigh dose-rate (FLASH) radiotherapy:
625 a topical review”. In: (2020). DOI: <https://doi.org/10.1088/1361-6560/abaa28>.
- 626 [10] Fabio Di Martino et al. “FLASH Radiotherapy With Electrons: Issues Related to
627 the Production, Monitoring, and Dosimetric Characterization of the Beam”. In:
628 *Frontiers in Physics* 8 (2020). ISSN: 2296-424X. DOI: [10.3389/fphy.2020.570697](https://doi.org/10.3389/fphy.2020.570697).
629 URL: <https://www.frontiersin.org/articles/10.3389/fphy.2020.570697>.
- 630 [11] M. Dyndal et al. “Mini-MALTA: Radiation hard pixel designs for small-electrode
631 monolithic CMOS sensors for the High Luminosity LHC”. In: (2019). DOI: <https://doi.org/10.1088/1748-0221/15/02/p02005>.
- 633 [12] M. Barbero. “Radiation hard DMAPS pixel sensors in 150 nm CMOS technology
634 for operation at LHC”. In: (2020). DOI: <https://doi.org/10.1088/1748-0221/15/05/p05013>.
- 636 [13] K. Moustakas et al. “CMOS Monolithic Pixel Sensors based on the Column-Drain
637 Architecture for the HL-LHC Upgrade”. In: (2018). DOI: <https://doi.org/10.1016/j.nima.2018.09.100>.

- 639 [14] I. Caicedo et al. “The Monopix chips: depleted monolithic active pixel sensors with
640 a column-drain read-out architecture for the ATLAS Inner Tracker upgrade”. In:
641 (2019). DOI: <https://doi.org/10.1088/1748-0221/14/06/C06006>.
- 642 [15] D. Kim et al. “Front end optimization for the monolithic active pixel sensor of the
643 ALICE Inner Tracking System upgrade”. In: *JINST* (2016). DOI: doi:10.1088/
644 1748-0221/11/02/C02042.
- 645 [16] L. Pancheri et al. “A 110 nm CMOS process for fully-depleted pixel sensors”. In:
646 (2019). DOI: <https://doi.org/10.1088/1748-0221/14/06/c06016>.
- 647 [17] L. Pancheri et al. “Fully Depleted MAPS in 110-nm CMOS Process With 100–300-
648 um Active Substrate”. In: (2020). DOI: 10.1109/TED.2020.2985639.